Real-Space Interpretation of Interatomic Charge Transfer and Electron Exchange Effects by Combining Static and Kinetic Potentials and Associated Vector Fields

Sergey A. Shteingolts,[a] *Adam I. Stash*,[b] *Vladimir G. Tsirelson*,[c,d] *and Robert R. Fayzullin* [a] *

[a] Arbuzov Institute of Organic and Physical Chemistry, FRC Kazan Scientific Center, Russian Academy of Sciences, 8 Arbuzov Street, Kazan 420088, Russian Federation

[b] A.N. Nesmeyanov Institute of Organoelement Compounds of Russian Academy of Sciences, 28 Vavilov Street, Moscow 119991, Russian Federation

[c] D.I. Mendeleev University of Chemical Technology, 9 Miusskaya Square, Moscow 125047, Russian Federation

[d] South Ural State University, 76 Lenin Avenue, Chelyabinsk, 454080, Russian Federation

ABSTRACT: Intricate behavior of one-electron potentials from the Euler equation for electron density and corresponding gradient force fields in crystals was studied. Bosonic and fermionic quantum potentials were utilized in bonding analysis as descriptors of the localization of electrons and electron pairs. Channels of locally enhanced kinetic potential and the corresponding saddle Lagrange points were found between chemically bonded atoms linked by the bond paths. Superposition of electrostatic $\varphi_{es}(\boldsymbol{r})$ and kinetic $\varphi_{k}(\boldsymbol{r})$ potentials and electron density $\rho(\boldsymbol{r})$ allowed partitioning any molecules and crystals into atomic ρ- and potential-based φ-basins; the

φ_k-basins explicitly account for electron exchange effect, which is missed for φ_{es}-ones. Phenomena of interatomic charge transfer and related electron exchange were explained in terms of space gaps between ρ- and φ-zero-flux surfaces. The gap between φ_{es}- and ρ-basins represents the charge transfer, while the gap between φ_k- and ρ-basins is proposed to be a real-space manifestation of sharing the transferred electrons. The position of φ_k-boundary between φ_{es}- and ρ-ones within an electron occupier atom determines the extent of electron sharing. The stronger an H···O hydrogen bond is, the deeper hydrogen atom's φ_k-basin penetrates oxygen atom's ρ-basin. For covalent bonds, a φ_k-boundary closely approaches a φ_{es}-one indicating almost complete sharing the transferred electrons, while for ionic bonds, the same region corresponds to electron pairing within the ρ-basin of an electron occupier atom.

INTRODUCTION

The topological atom as an open quantum system is the central notion of the quantum theory of atoms in molecules and crystals (QTAIMC).[1–5] It is defined as an electron-density region of space Ω around a nucleus enclosed with a surface $S(\Omega, \boldsymbol{r}_s)$, at every point of which the local flux of gradient of electron density is equal to zero (a zero-flux condition): $\nabla\rho(\boldsymbol{r}) \cdot \mathbf{n}(\boldsymbol{r}) = 0$, $\forall \boldsymbol{r} \in S(\Omega, \boldsymbol{r}_s)$; $\mathbf{n}(\boldsymbol{r})$ is the unit normal vector directed outward. The physical content of quantum atoms has been explained by Richard Bader with coauthors and this concept is widely used today.[6–9] As a result, a molecule or a crystal is seen as a set of non-overlapping space-filling atomic-like fragments defined by the vector $\nabla\rho(\boldsymbol{r})$-field, which are termed ρ-basins. In this field, critical points (CPs), i.e., points where $\nabla\rho(\boldsymbol{r}) = 0$, are present. A saddle CP (3, –1), also called a bond critical point (BCP), and a respective bond path, formed by two gradient lines emitted from this BCP and terminated on two neighboring atoms, are considered in QTAIMC as indicators that these atoms

are (topologically) bonded to each other.[10] Each bond path is mirrored by a virial path, a line of minimal electronic potential energy density $v(\boldsymbol{r})$ connecting these atoms.[11] Both of these paths recover the expected chemical connectivity. Tsirelson[12] and Martín Pendás et al.[13] indicated that the bond paths are accompanied by the presence of privileged exchange energy density channels. Later we noted that bond paths are also accompanied by correlation energy density bridges[14,15] and a local decrease of electronic temperature.[15–17] At the same time, it was stated that a lack of a bond path between any two approximate atoms does not necessarily mean that corresponding interatomic interaction is absent.[18–21] Also, there are a number of phenomena, as the interatomic charge transfer, electron sharing, and exchange effects, which are not clearly represented in real space in terms of QTAIMC ρ-atoms.

To get more insight into the mechanisms of chemical bond formation beyond the orthodox topological analysis of electron density (ED) $\rho(\boldsymbol{r})$, we focus in this work on the analysis of electronic potentials $\varphi_i(\boldsymbol{r})$ and corresponding local forces $\boldsymbol{F}_i(\boldsymbol{r})$[15,22,23] within the framework of quantum crystallography.[24–31] The orbital-free branch of quantum crystallography makes it possible to operate with ED and its derivatives, obtained either from theoretical calculations or experimental diffraction data for a many-electron multinuclear system in the stationary ground state. Each component of the inner potential field can be expressed starting from the one-electron Euler equation for ED:[22,23]

$$\mu[\rho(\boldsymbol{r})] = \frac{\delta E_k[\rho(\boldsymbol{r})]}{\delta\rho(\boldsymbol{r})} + \varphi_{em}(\boldsymbol{r}).$$

Here $\mu(\boldsymbol{r})$ is the chemical potential, i.e., the path-independent work that needs to be done for moving any electron belonging to a system from infinity to a reference point against the kinetic force field and the static Coulomb force field corrected for exchange.[22,32–34] Functional $E_k[\rho]$ describes the noninteracting kinetic energy of electrons. In one-determinant approximation, the

latter can be presented as the sum of Pauli $E_P[\rho]$ and von Weizsäcker $E_W[\rho]$ kinetic energy functionals.[35–37] Naturally, the kinetic potential $\varphi_k(\boldsymbol{r})$ can also be written as the sum of Pauli $\varphi_P(\boldsymbol{r})$ and von Weizsäcker $\varphi_W(\boldsymbol{r})$ potentials: $\varphi_k(\boldsymbol{r}) = \varphi_P(\boldsymbol{r}) + \varphi_W(\boldsymbol{r})$.[38] The von Weizsäcker potential $\varphi_W(\boldsymbol{r})$ is the spin-independent potential, which arises from the structure confinement restrictions and the quantum electron fluctuations due to Heisenberg's uncertainty principle. It can be directly computed from $\rho(\boldsymbol{r})$: $\varphi_W(\boldsymbol{r}) = (1/8) \cdot |\nabla\rho(\boldsymbol{r})|^2/\rho^2(\boldsymbol{r}) - (1/4) \cdot \nabla^2\rho(\boldsymbol{r})/\rho(\boldsymbol{r})$ and reflects the allowed atomic electron-shell structure.[39–42] Based on Hunter's works,[39,43] the positive and negative values of $\varphi_W(\boldsymbol{r})$ indicate the areas where classic electron motion is allowed or prohibited, respectively. The Pauli potential $\varphi_P(\boldsymbol{r})$ describes the increase in the total kinetic energy density of electrons as compared to spinless particles, i.e., represents a correction to $\varphi_W(\boldsymbol{r})$ originating from the antisymmetry requirement for the many-electron wavefunction.[37,44–47] Note that $\varphi_P(\boldsymbol{r})$ is not defined in the regions populated by less than 2 electrons, for example, close to the positions of hydrogen atoms.[15,23]

The static one-electron potential acting on an electron in a molecule (PAEM) $\varphi_{em}(\boldsymbol{r})$ is the negative average local potential energy of any one internal electron at a reference position in the field of nuclei and remaining electrons of a system:[48–51]

$$\varphi_{em}(\boldsymbol{r}) = -\varphi_{es}(\boldsymbol{r}) + \varphi_x(\boldsymbol{r}).$$

Here, $-\varphi_{es}(\boldsymbol{r})$ is the electronic electrostatic potential, which characterizes the Coulomb interaction between a negatively charged electron at a point $\boldsymbol{r}$ with nuclei and the rest of electrons, and $\varphi_x(\boldsymbol{r})$ is the static exchange potential.

Combining the expressions for $\varphi_k(\boldsymbol{r})$ and $\varphi_{em}(\boldsymbol{r})$, Tsirelson and Stash have recently presented the one-electron Euler equation in the following form:[22]

$$\mu(\boldsymbol{r}) = \varphi_k(\boldsymbol{r}) + \varphi_{em}(\boldsymbol{r}) = \varphi_P(\boldsymbol{r}) + \varphi_W(\boldsymbol{r}) - \varphi_{es}(\boldsymbol{r}) + \varphi_x(\boldsymbol{r}).$$

All components of kinetic and static forces may be linked to their corresponding potentials as follows: $\boldsymbol{F}_i(\boldsymbol{r}) = -\nabla\varphi_i(\boldsymbol{r})$ and $\mathcal{F}(\boldsymbol{r}) = -\nabla\varphi_{em}(\boldsymbol{r})$. Notably, since $\varphi_{es}(\boldsymbol{r})$ normally considers a unit test positive charge external to a system, the electrostatic force for electrons belonging to a system is $\boldsymbol{F}_{es}(\boldsymbol{r}) = \nabla\varphi_{es}(\boldsymbol{r})$. The chemical potential for a stable system is constant $\mu(\boldsymbol{r}) = \mu$, therefore the net local force acting on any electron in a system is zero everywhere: $\boldsymbol{F}_\mu(\boldsymbol{r}) = -\nabla\mu(\boldsymbol{r}) = 0$. From this, the following expression can be obtained: $\boldsymbol{F}_\mu(\boldsymbol{r}) = \boldsymbol{F}_k(\boldsymbol{r}) + \mathcal{F}(\boldsymbol{r}) = 0$. The heterotropic force of kinetic nature $\boldsymbol{F}_k(\boldsymbol{r}) = \boldsymbol{F}_P(\boldsymbol{r}) + \boldsymbol{F}_W(\boldsymbol{r})$ pushes electrons away from the atomic nuclei, while the homotropic static force acting on an electron in a molecule (FAEM) $\mathcal{F}(\boldsymbol{r}) = \boldsymbol{F}_{es}(\boldsymbol{r}) + \boldsymbol{F}_x(\boldsymbol{r})$ draws electrons toward atomic nuclei. The balance of these forces is responsible for the existence of stable heterogeneous electron continuum. It should be noted that Martín Pendás with co-workers have shown that FAEM $\mathcal{F}(\boldsymbol{r})$ is similar to the non-gradient one-electron Ehrenfest force field $\mathfrak{F}(\boldsymbol{r})$.[52,53]

Among all the above-mentioned potentials, the electrostatic and kinetic ones, $\varphi_{es}(\boldsymbol{r})$ and $\varphi_k(\boldsymbol{r})$, show their respective atomic-like potential-based φ-basins determined by the zero-flux condition by analogy with atomic ρ-basins:

$$\boldsymbol{F}_{es}(\boldsymbol{r}) \cdot \mathbf{n}(\boldsymbol{r}) = \nabla\varphi_{es}(\boldsymbol{r}) \cdot \mathbf{n}(\boldsymbol{r}) = 0, \quad \forall \boldsymbol{r} \in U(\Omega, \boldsymbol{r}_U),$$

$$\boldsymbol{F}_k(\boldsymbol{r}) \cdot \mathbf{n}(\boldsymbol{r}) = -\nabla\varphi_k(\boldsymbol{r}) \cdot \mathbf{n}(\boldsymbol{r}) = 0, \quad \forall \boldsymbol{r} \in P(\Omega, \boldsymbol{r}_P).$$

Here, $\boldsymbol{F}_{es}(\boldsymbol{r})$ and $\boldsymbol{F}_k(\boldsymbol{r})$ are the corresponding local electrostatic and kinetic forces acting on an electron, while $U(\Omega)$ and $P(\Omega)$ are the zero-flux surfaces or boundaries limiting φ_{es}- and φ_k-basins; $\mathbf{n}(\boldsymbol{r})$ is the normal unit vector directed outward. Within these basins, according to their physical nature, the electronic forces $\boldsymbol{F}_{es}(\boldsymbol{r})$ and $\boldsymbol{F}_k(\boldsymbol{r})$ act toward and away from the position of atomic nuclei, respectively. In turn, these two forces are generated by the electrostatic partial charge density $q_{es}(\boldsymbol{r})$ and the sum of Pauli $q_P(\boldsymbol{r})$ and von Weizsäcker $q_W(\boldsymbol{r})$ partial charge

densities, respectively.[23] The scalar fields $\varphi_{es}(\boldsymbol{r})$ and $\varphi_{k}(\boldsymbol{r})$ in molecules and crystals features four types of CPs where $\nabla\varphi_{es}(\boldsymbol{r}) = 0$ or $\nabla\varphi_{k}(\boldsymbol{r}) = 0$.[22,54] As for ED, these points are associated with maxima (3, –3), line and ring saddle points (3, –1) and (3, +1), and minima (3, +3). For the $\varphi_{es}(\boldsymbol{r})$ and $\varphi_{k}(\boldsymbol{r})$ potentials, the same critical points are in fact Lagrange points, where the corresponding force $\boldsymbol{F}_{es}(\boldsymbol{r})$ or $\boldsymbol{F}_{k}(\boldsymbol{r})$ is equal to zero.[22,55] In the $\nabla\varphi_{es}$- and $\nabla\varphi_{k}$-fields, there are φ_{es}- or φ_{k}-paths, each of which consists of a pair of gradient lines originating at a CP (3, –1) and terminating at two neighboring CPs (3, –3).[15] 3D attractors of the electronic force fields, i.e., CPs (3, –3), coincide with positions of atomic nuclei, which allows one to attribute considered φ-basins to specific atoms within a molecule or a crystal. At that, φ_{es}-basins enclose all electric field lines starting at corresponding nuclei and define electrically neutral pseudoatoms.[56] According to Green's theorem, the total integrated charges over φ_{es}-basins are equal to zero and φ_{es}-boundary can be viewed as an electrostatic shield preventing the accessibility of any external charge inside a φ_{es}-basin and any internal charge outside it. The topology of $\varphi_{es}(\boldsymbol{r})$[54,57,58] in combination with ρ-basins is widely employed for describing electrostatic contribution for various interactions in associates and crystals.[14,15,66,17,59–65] Further, the gap between φ_{es}- and ρ-basins is attributed to phenomena of interatomic charge (electron) transfer and can be used to estimate it.[15] However, although φ_{k}-basins (pseudoatoms) and corresponding kinetic force field have a robust physical definition, it is not clear for now how it can be exploited to retrieve chemical information.[15,17,22,67]

Recently, the local electronic potentials and corresponding gradient forces have been successfully employed for the chemically accessible yet physically robust description of chemical bonding.[15] The examination of electronic potentials can serve to enhance or even substitute the use of existing chemical descriptors: for example, the analysis of $\varphi_{em}(\boldsymbol{r})$ can be considered as a viable or even preferable alternative to $\varphi_{es}(\boldsymbol{r})$.[15,66] Nevertheless, it is worth noting the widespread use of

$\varphi_{es}(\boldsymbol{r})$ for the explanation and prediction of chemical behavior.[68–76] The Pauli potential $\varphi_P(\boldsymbol{r})$ displays similar features to electron localization function (ELF), although its more complex nature and detailed distribution demands proper interpretation.[15,46] Lastly, the von Weizsäcker potential $\varphi_W(\boldsymbol{r})$ or related one-electron potential is an alternative to the Laplacian of ED $\nabla^2\rho(\boldsymbol{r})$,[15,42,62,63,77,78] which is just the empirical measure of electron concentration or depletion via ED topology.[79] Modest attempts have been made to link the behavior of the potentials with essential chemical concepts, such as interatomic interaction, charge transfer, electron lone pair, and donor-acceptor (Lewis) mechanism of noncovalent bonds.[15]

In this work, we generalize the described methodology to different kinds of chemical bonds present in a diverse set of selected crystals, including polar and nonpolar covalent bonds, ionic ones, classical and nonclassical hydrogen bonds, as well as several weak to moderate intermolecular interactions. By combining the approach of superposing ρ- and φ-basins with the study of the behavior of electronic potentials and corresponding forces, we arrived at a phenomenological partitioning scheme of many-nuclear many-electron systems, which enables us to further understand the complex atomic structure of electron occupier revealed by different basin boundaries and phenomena of charge transfer and subsequent exchange, electron sharing, and chemical bonding. We aimed to obtain a unified picture, which enhances the understanding of fuzzy chemical concepts utilizing the robust, physically grounded functions, which in turn can be obtained solely from the (experimental) ED distribution.

RESULTS

Properties of atomic and potential-based basins

We start by discussing the differences in shape, volume, and charge of atomic ρ- and potential-based φ-basins for the chosen model crystalline compounds: oxalic acid dihydrate, isocyanuric acid derivative (*ica*; see Scheme S1), sodium chloride, and high-temperature superconductor magnesium diboride. Conventional ED analysis for these compounds was carried out earlier.[17,80,81] Figures 1 and S1 depict the three types of ρ- and φ-basins for the studied compounds and Table S1 summarizes their characteristics. The first significant difference between the basin types is their relative space volume. We observe the following strong trend: in the series of basin types from ρ- through φ_k- to φ_{es}-ones, the volumes of more electronegative atoms become smaller, while the ones of electropositive atoms increase. For instance, for the atoms O1 and H1 in the oxalic acid molecule, these volumes are equal to 15.85, 12.00, and 6.79 Å^3 for the oxygen atom and 1.20, 4.30, and 8.66 Å^3 for the hydrogen atom. This trend is clearly visible in Figure 1a-c. The ionic compounds, such as NaCl, give even more contrasting examples (Figure 1d-i). For the Na atom in the salt, the volume of its φ_{es}-basin (27.12 Å^3) is almost three times larger than its ρ-basin (9.41 Å^3), with the φ_k-basin volume having an intermediate value of 17.28 Å^3. At the same time, the volumes of ρ-, φ_k-, and φ_{es}-basins of the Cl atom are diminishing as 34.59, 26.73, and 16.90 Å^3, respectively. Note meaningful distinction between molecular and atomic/ionic crystals: for the former, the change in volume between different basin types occurs mostly in the intermolecular region, while in NaCl and MgB_2 no outer regions can be practically distinguished (except for B···B contacts between graphene-like boron layers). Hence, the volumes of atomic and potential basins for covalent and ionic network solids change rather evenly in all directions. Figure 1g-i shows that the QTAIMC atoms of Mg are isolated from each other being placed above and below the six-membered rings of the boron layers. Interestingly, the described regularity leads to the fact that

φ_k- and φ_{es}-pseudoatoms of Mg in MgB_2 are already in contact and even docked (mainly in a plane parallel to the boron plane), respectively.

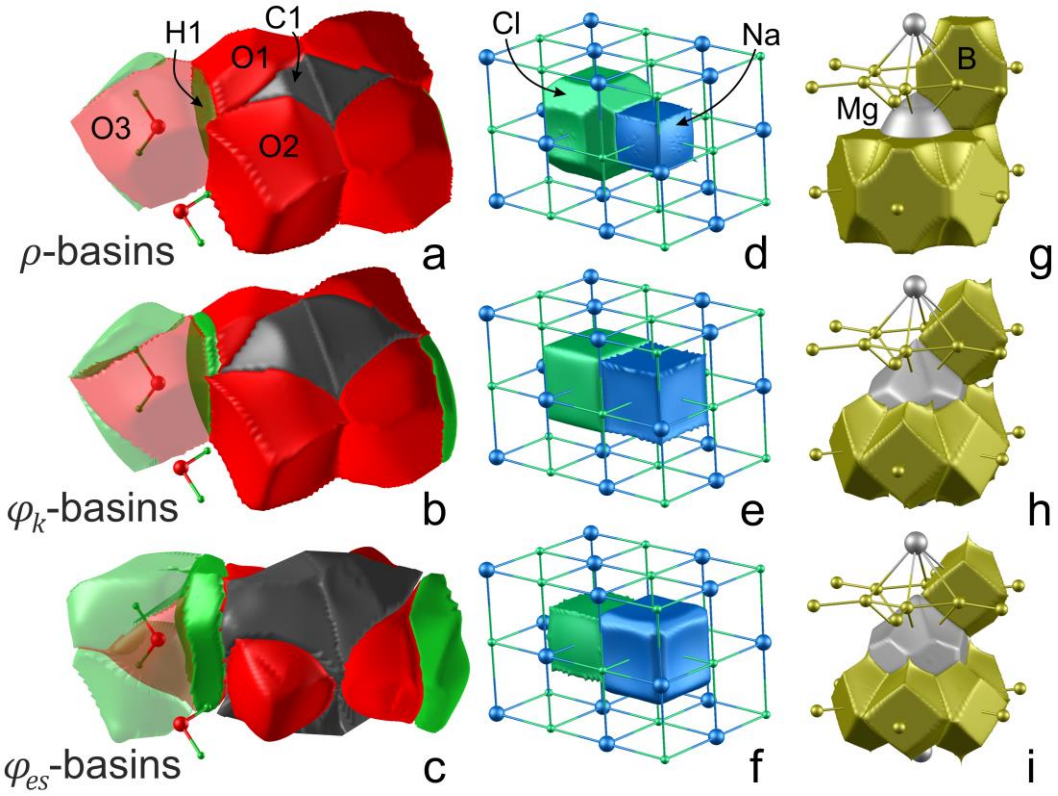

Figure 1. Atomic ρ-basins (first row) and potential-based φ_k- and φ_{es}-basins (second and third rows) for the molecular crystal of $(COOH)_2 \times 2H_2O$ (a-c) and the ionic and covalent network solids of NaCl (d-f) and MgB_2 (g-i).

A similar regular trend is observed for integrated charges over ρ- and φ-basins Q_i (Table S1). In the series of ρ-, φ_k-, and φ_{es}-basins, (pseudo)atomic charges decrease in their absolute value so that φ_k-basins are always less charged than ρ-basin. For example, in the oxalic acid molecule, the electronegative oxygen atom O1 shows the following charges: Q_ρ = –1.05 e, Q_k = –0.28 e, and Q_{es} = 0 e, while for the electropositive carbon atom C1 they are equal to +1.43, +0.31,

and 0 e, respectively. Similar results, i.e., smaller charges compared to ρ-basins, were obtained after the integration of $\rho(\boldsymbol{r})$ over the Ehrenfest force field pseudoatoms.[52]

The shapes of ρ- and φ-basins depend on the type of crystal structure. For the molecular crystals of oxalic acid dihydrate and *ica*, the molecular shapes constructed out of ρ- and φ_k-basins are very similar and are characterized by the rather sharp edges and planar faces from the sides of formed intermolecular interactions. This is not the case for φ_{es}-basins, which in general have more smooth, rounded surfaces, which is especially evident from the shapes of the oxygen atoms in the oxalic acid molecule in Figure 1c. An even more contrasting example is φ_{es}-basins of the sulfonyl atoms O1 and O3 and carbonyl atoms O2, O4, and O6 in the *ica* molecule shown in Figure S1, which have an almost ideal hemisphere shape, while still retaining the planar faces directed perpendicularly to the S=O and C=O bond lines. At the same time, hydrogens' φ_{es}-basins show concave regions imprinted due to the contact with the mentioned oxygens' φ_{es}-basins within a dense crystal packing of the molecules. The opposite can be observed for the ionic/atomic crystals of NaCl and MgB_2, for which φ_k- and φ_{es}-basins appeared to be more similar. In particular, the φ-basins of the Cl atom have a simple cubic shape, while its ρ-basin features additional pronounced faces corresponding to the Cl···Cl interaction. Conversely, the Na atom retains its cubic shape in all three studied functions with slightly more rounded edges in the case of φ_{es}-basins. The atomic ρ-basin of the Mg atom has a shape of a spinning top with no discernable faces, while its potential φ_k- and φ_{es}-basins have sharp edges and flat faces corresponding to the Mg···B bonds.

Shared interactions and electron pairs

Figure 2 features one-dimensional profiles of a complete set of the one-electron potentials included in the Euler equation for ED along the selected bond paths in the *ica* molecule. For the sake of comparison, analogous plots for the polar covalent bonds C8–O9 and C2–N1 are given in Figure S2. We start by discussing the static potential acting on an electron in a molecule $\varphi_{em}(\boldsymbol{r}) = -\varphi_{es}(\boldsymbol{r}) + \varphi_{x}(\boldsymbol{r})$ and electronic electrostatic potential $-\varphi_{es}(\boldsymbol{r})$. First, one can notice that the graphs of $-\varphi_{es}(\boldsymbol{r})$ and $\varphi_{em}(\boldsymbol{r})$ are of almost parabolic shape revealing barriers that separate two interacting atoms; the PAEM barrier appears to be noticeably lower due to accounting for the electron exchange. The higher φ_{es}- and φ_{em}-barriers, the harder it is for electrons to move from one atom to the other. For the nonpolar C–C and C–S covalent bonds (Figure 2a,b), the maxima of $-\varphi_{es}(\boldsymbol{r})$ and $\varphi_{em}(\boldsymbol{r})$ on the graphs, which correspond to the positions of Lagrange CP (3, –1) in $\varphi_{es}(\boldsymbol{r})$ and Lagrange CP (3, +1) in $\varphi_{em}(\boldsymbol{r})$, are located very close to the corresponding BCP. Recall that CPs (3, +1) in $\varphi_{em}(\boldsymbol{r})$ coincide with Lagrange CPs (3, –1) in $\varphi_{k}(\boldsymbol{r})$.[22] On the other hand, for the polar covalent bonds C–N, C=O, and S=O (Figures 2c,d and S2), a noticeable shift of $-\varphi_{es}(\boldsymbol{r})$ and $\varphi_{em}(\boldsymbol{r})$ maxima away from the BCP to the nucleus of the more electronegative atoms is observed. Moreover, a very slight shift of $-\varphi_{es}(\boldsymbol{r})$ and $\varphi_{em}(\boldsymbol{r})$ maxima relative to each other with the maximum of $\varphi_{em}(\boldsymbol{r})$ being a little closer to the BCP can be also seen. So, the asymmetry of φ_{es}- and φ_{em}-barriers can be distinguished for the highly polar S=O bond. This shift is governed by the shape of $\varphi_{x}(\boldsymbol{r})$ distribution. For the nonpolar bonds, the exchange potential $\varphi_{x}(\boldsymbol{r})$ features an almost flat plateau in the middle of the interatomic region. It yields a nearly constant correction to $-\varphi_{es}(\boldsymbol{r})$, and the maxima of $-\varphi_{es}(\boldsymbol{r})$ and $\varphi_{em}(\boldsymbol{r})$ are therefore aligned. Conversely, for the polar bonds, especially S=O, $\varphi_{x}(\boldsymbol{r})$ is distributed more unevenly, with the linear segment of the graph tilted down toward the electronegative atom. Hence, the CP (3, –1) in $\varphi_{es}(\boldsymbol{r})$ are located nearby the CP (3, +1) in $\varphi_{em}(\boldsymbol{r})$ and further away from the BCP, thus leading

to the strict sequence of the saddle critical points along a heteroatomic internuclear line. Looking ahead, this sequence is preserved and even more obvious for polar noncovalent bonds.

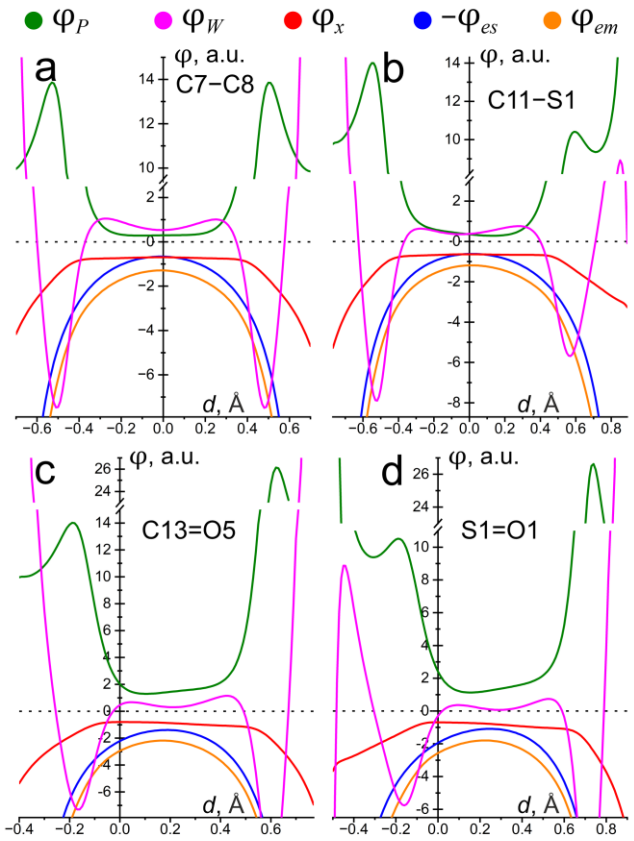

Figure 2. Behavior of Pauli $\varphi_P(\boldsymbol{r})$ (green), von Weizsäcker $\varphi_W(\boldsymbol{r})$ (magenta), exchange $\varphi_x(\boldsymbol{r})$ (red), and inverted electrostatic $-\varphi_{es}(\boldsymbol{r})$ (blue) potentials and static potential acting on an electron in a molecule $\varphi_{em}(\boldsymbol{r})$ (orange) along the bond paths of the nonpolar and polar covalent bonds in *ica*. Zero value on the abscissa axes denotes the location of corresponding BCPs.

Since the kinetic potential $\varphi_k(\boldsymbol{r})$ is equal to $-\varphi_{em}(\boldsymbol{r}) + \mu$, it is topologically inverted relative to $\varphi_{em}(\boldsymbol{r})$. So, let us now move to the discussion of its constituents, namely the von Weizsäcker $\varphi_W(\boldsymbol{r})$ and Pauli $\varphi_P(\boldsymbol{r})$ potentials. The former variates its sign along the bond paths thus reflecting the electronic shell structure. Reinterpreting the results presented for the one-electron potential by Hunter,[39] it can be argued that, in the regions of positive and negative $\varphi_W(\boldsymbol{r})$,

the electron motion is classically allowed and forbidden, respectively. From the expression for $\varphi_W(\boldsymbol{r})$, it follows that the regions of $\varphi_W(\boldsymbol{r}) > 0$ correspond to valence shell charge concentrations (VSCCs), where generally $\nabla^2\rho(\boldsymbol{r}) < 0$. Conversely, if $\varphi_W(\boldsymbol{r}) < 0$, the positive Laplacian contribution dominates and electron depletion occurs. For our examples (Figures 2 and S2), the outer valence region, indicated by the positive values of $\varphi_W(\boldsymbol{r})$, is separated by one (for the C, N, and O atoms) or two (for the S atom) deep negative peaks from the inner electron shells. Within this outer valence region, the two individual VSCCs merge at the midpoint of covalent bonds, where a local positive $\varphi_W(\boldsymbol{r})$ minimum is observed. Thus, the von Weizsäcker force $\boldsymbol{F}_W(\boldsymbol{r})$ in this narrow region acts toward this local minimum rather close to the BCP. The one-dimensional distribution of always positive $\varphi_P(\boldsymbol{r})$ along the bond paths also reveals the atomic electronic shells, which is evident by the alternating series of local potential minima and maxima. Within the inner electronic shells, local maxima of $\varphi_P(\boldsymbol{r})$ are positioned closely to the minima of $\varphi_W(\boldsymbol{r})$ and represent the regions where the same-spin electron repulsion is high. The important characteristic of $\varphi_P(\boldsymbol{r})$ is that it features a wide, nearly flat segment of minimal potential in the center of covalent bonds at least on the scale in question, which manifests localization of shared electron pair(s) in the middle part of interatomic regions. Compared with the previously discussed functions, the distribution of $\varphi_P(\boldsymbol{r})$ noticeable variates depending on the types of atoms forming a covalent bond. For example, in the case of the homoatomic C–C bond (Figure 2a), the region of the lowest Pauli potential is nearly flat and parallel to the abscissa axis, while for the C–S bond (Figure 2b) the minimum of $\varphi_P(\boldsymbol{r})$ is slightly shifted toward the sulfur atom. Generally, for the more polar C–N, C=O, and S=O covalent bonds (Figures 2c,d and S2), the minimum within the wide potential well is located near the corresponding BCP and consequently is shifted to the electropositive atom. At the same time, it is observed a slight rise of $\varphi_P(\boldsymbol{r})$ inside the well toward the region of VSCC with

a large value of $\varphi_W(\boldsymbol{r})$, i.e., to the electronegative atom. The corresponding Pauli force $\boldsymbol{F}_P(\boldsymbol{r})$ acts on the electrons in the direction of potential minimum, pushing them toward the center of a covalent bond and promoting the sharing of electrons between two atoms. Strictly speaking, for the polar covalent bonds $\varphi_P(\boldsymbol{r})$ exhibits a very small hill of increased potential in the midpoint of the mentioned segment (see Figure S2), which is significantly smaller than the corresponding minimum of $\varphi_W(\boldsymbol{r})$.

For all studied covalent bonds, φ_{es}- and φ_{em}-barriers are relatively low, while both $\varphi_W(\boldsymbol{r})$ and $\varphi_P(\boldsymbol{r})$ show pronounced positive minima at the center of interatomic regions. Previously, we noted that according to the widely accepted classifications of the interactions types,[82,83] based on the sign of $\nabla^2\rho(\boldsymbol{r})$ at the BCP, the S=O bond in *ica* can be formally attributed to the intermediate interaction (not the shared one),[17] similar to strong hydrogen bonds. In our opinion, this goes against general chemical intuition. Meanwhile, the behavior of $\varphi_W(\boldsymbol{r})$ and $\varphi_P(\boldsymbol{r})$ confirms that, in fact, the S=O bond is not basically different from any other covalent ones. Figure S3 presents the distributions of various functions along the S=O line. In particular, we note below that the distinguishing feature of noncovalent interactions is the presence of both pronounced Pauli barrier, i.e., a local positive maximum of $\varphi_P(\boldsymbol{r})$ instead of continuous plateau of minimal potential observed for covalent bonds, and wide and deep well of negative $\varphi_W(\boldsymbol{r})$ in the middle of interactions. We conclude that joined analysis of electronic potentials, especially combination of the two mentioned above, not only can be successfully used for the description of electronic shell structure but also should be utilized for classification of the interaction types.

Figure 3 shows the vector fields $\boldsymbol{F}_W(\boldsymbol{r})$, $\boldsymbol{F}_P(\boldsymbol{r})$, and $\boldsymbol{F}_k(\boldsymbol{r})$ constructed in the three-dimensional layer containing the oxalic acid and water molecules in the crystal. It should be noted that the magnitudes of static FAEM $\mathcal{F}(\boldsymbol{r})$ and kinetic force $\boldsymbol{F}_k(\boldsymbol{r})$ are equal, but the forces act

oppositely. The observed picture supports the previously made findings regarding the directions of the considered forces. All these forces have the highest values near the atomic nuclei and decrease with the distance from it. However, while the kinetic force $\boldsymbol{F}_k(\boldsymbol{r})$ at any point within the system is always directed away from the closest atomic nucleus, both von Weizsäcker $\boldsymbol{F}_W(\boldsymbol{r})$ and Pauli $\boldsymbol{F}_P(\boldsymbol{r})$ forces have their direction governed by the local ED features, e.g., VSCCs and ED depletions or shared and lone electron pairs. Figure 3b clearly shows the vector vortices characterized by the near-zero magnitudes (indicated by blue arrows) in the Pauli force field on both sides of the oxygen atom O2 in the nonbonding region within its ρ-basin, which correspond to the formation of two lone electron pairs in the plane of the oxalic acid molecule under the action of $\boldsymbol{F}_P(\boldsymbol{r})$. As a further example, let us consider the ordinary C–C covalent bond. Within its interatomic region, $\boldsymbol{F}_W(\boldsymbol{r})$ has two clear points of origin at approximately ⅓ and ⅔ of the bond's length, which are aligned with the local maxima of $\varphi_W(\boldsymbol{r})$ found for the similar C–C bond in *ica* (Figure 2a). From these two points $\boldsymbol{F}_W(\boldsymbol{r})$ acts toward the BCP in the direction of local $\varphi_W(\boldsymbol{r})$ minimum and toward the atomic nuclei further from the bond midpoint. The apparent magnitude of $\boldsymbol{F}_W(\boldsymbol{r})$ on the considered bonds is noticeably different from zero, averaging at ca. 2 a.u. Conversely, $\boldsymbol{F}_P(\boldsymbol{r})$ shows a near-zero magnitude for the most part of the C–C line and quickly rises to its maximum value not far from the carbon nuclei. $\boldsymbol{F}_P(\boldsymbol{r})$ is directed from the carbon atoms and vicinity around the bond to the BCP. This once again is fully consistent with the flat linear section followed by a steep increase on both sides on the $\varphi_P(\boldsymbol{r})$ graph (Figure 2a). For the polar bonds, the behavior of $\boldsymbol{F}_W(\boldsymbol{r})$ and $\boldsymbol{F}_P(\boldsymbol{r})$ is similar, although more intricate. As opposed to the previous two, the magnitude of $\boldsymbol{F}_k(\boldsymbol{r})$ uniformly increases from its minimum (ca. 1 a.u. for the C–C bond) at the center toward the nuclear positions, which is consistent with the parabolic shape of $\varphi_k(\boldsymbol{r})$ and $\varphi_{em}(\boldsymbol{r})$ graphs for chemical bonds. We can conclude that the formation of the actual

electronic structure of the crystal occurs with the decisive role of the kinetic factor, which has a quantum nature.

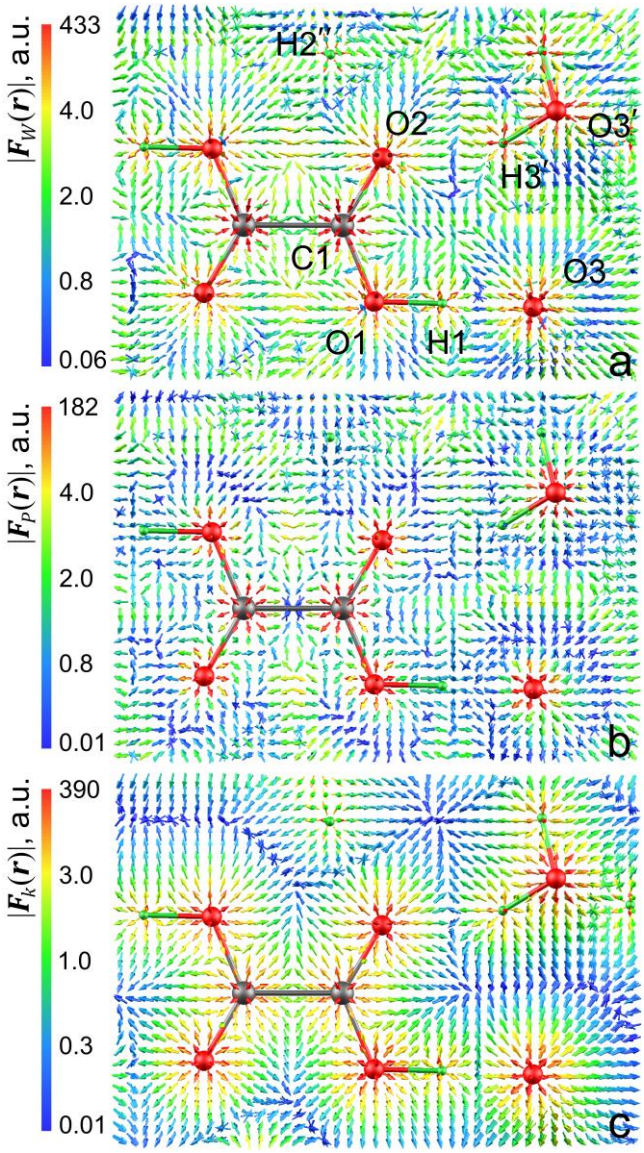

Figure 3. Static vector fields $\boldsymbol{F}_W(\boldsymbol{r})$ (a), $\boldsymbol{F}_P(\boldsymbol{r})$ (b), and $\boldsymbol{F}_k(\boldsymbol{r})$ (c) calculated for the oxalic acid dihydrate crystal in the layer with a thickness of 1 Å. Arrows are colored according to the force magnitude and indicate the direction of the forces at the center of each arrow. For a slightly different orientation of the $\boldsymbol{F}_k(\boldsymbol{r})$ distribution see Figure S4.

The distinguishing feature of the $\boldsymbol{F}_k$-field is its ability to provide an apparent (statistically equilibrium) molecular shape. The latter is manifested by the significantly large regions of near-zero force located in the intermolecular area. These regions form a continuous enclosed surface of near-zero $\boldsymbol{F}_k(\boldsymbol{r})$, which naturally closely resembles the molecular shape constructed out of φ_k-basins. It should be noted that this approximate $\boldsymbol{F}_k$-surface is observed between molecular entities but not between covalently bonded atoms within a molecule. The same reasoning and conclusions are also valid for the static $\mathcal{F}$-field, which in turn resembles Ehrenfest force field $\mathfrak{F}(\boldsymbol{r})$.[52,53]

Following the notation from the recent article,[23] here we also utilize the decomposition of potentials from the Euler equation for ED, when the terms are grouped to distinguish electrostatic, quantum bosonic, and quantum fermionic contributions: $\mu(\boldsymbol{r}) = -\varphi_{es}(\boldsymbol{r}) + \varphi_b(\boldsymbol{r}) + \varphi_f(\boldsymbol{r})$. The quantum bosonic potential $\varphi_b(\boldsymbol{r})$ is exactly the von Weizsäcker potential $\varphi_W(\boldsymbol{r})$. The quantum fermionic potential $\varphi_f(\boldsymbol{r})$ is equal to the sum of Pauli $\varphi_P(\boldsymbol{r})$ and static exchange $\varphi_x(\boldsymbol{r})$ potentials and provides both repulsive and attractive local fermionic contributions to the electronic energy. The sign of $\varphi_f(\boldsymbol{r})$ indicates which effect dominates at that region of space: the spatial static electron exchange if the negative contribution of $\varphi_x(\boldsymbol{r})$ is greater or kinetic contribution due to Pauli effect if everywhere positive $\varphi_P(\boldsymbol{r})$ dominates. Figure 4 presents the distribution of $\varphi_b(\boldsymbol{r})$ and $\varphi_f(\boldsymbol{r})$ potentials in the planes of the ester (a, b) and ether (c, d) functional groups of the *ica* molecule. Similar to $\varphi_W(\boldsymbol{r})$ and $\varphi_P(\boldsymbol{r})$, both potentials $\varphi_b(\boldsymbol{r})$ and $\varphi_f(\boldsymbol{r})$ are able to reveal the atomic electronic shells. The radii from the nuclei to the inner boundary of the outer electronic shell, i.e., core electron region, can be distinguished, with the oxygen atoms having smaller K-L radii compared to the carbon atoms. For the ordinary C7–C8 covalent bond (Figure 4c, d), $\varphi_f(\boldsymbol{r})$ features a broad region of negative minimal potential in the midpoint, while $\varphi_b(\boldsymbol{r})$ instead displays two separate local maxima along the line between the carbon atoms' nuclei revealing bonding

VSCCs. For the polar C=O and C–O covalent bonds (Figure 4), no negative values of $\varphi_f(\boldsymbol{r})$ are observed in the internuclear region, with instead a single positive local maximum shifted in the direction of the electropositive carbon atom. Notably, the distribution of $\varphi_f(\boldsymbol{r})$ is very similar to $\varphi_P(\boldsymbol{r})$.[15,46] Potential $\varphi_b(\boldsymbol{r})$ exhibits two positive peaks of different heights: the higher peak near the oxygen atom and the lower one near the carbon atom. Probably, for recovering the location of either shared and lone electron pair(s) in terms of electronic potentials, it is reasonable to consider the region related to the VSCC with a larger value of $\varphi_b(\boldsymbol{r})$, which is simultaneously sited inside the rather wide Pauli potential well and shows lower possible values of $\varphi_P(\boldsymbol{r})$. For the carbonyl atom O5 in the nonbonding regions, potentials $\varphi_f(\boldsymbol{r})$ and $\varphi_b(\boldsymbol{r})$ display two negative and positive peaks, respectively, which correspond to the VSCCs or electron lone pairs lying in the plane of the ester group, as expected for an sp^2-hybridized oxygen atom (the similar case was considered in the term of force fields above in Figure 3b). For the sp^3-atoms O9 and O14, both functions successfully reveal regions containing the electron lone pairs situated above and below the map planes. There are distinct differences in the shape and area of the space occupied by the electron pairs described by these two potentials: $\varphi_b(\boldsymbol{r})$ rapidly decreases from the boundary of the core electrons, while $\varphi_f(\boldsymbol{r})$ represents the near-zero values of $\varphi_P(\boldsymbol{r})$, which corresponds to the slow increase of Pauli kinetic energy within the atomic basin. Importantly, the volumes occupied by the shared and lone electron pairs in the $\varphi_b(\boldsymbol{r})$ or $\varphi_W(\boldsymbol{r})$ notation are compressed and placed rather closer to the nuclei as compared to the $\varphi_f(\boldsymbol{r})$ and $\varphi_P(\boldsymbol{r})$ representations owing to account for the electron quantum spread (fluctuation), which is related to the electrostatic attraction of electrons to the nuclei. Interestingly, both functions feature the areas of near-zero values, which resemble in shape the atomic ρ- and φ_k-basins shown in Figure 5. Thus, recalling the clear physical meaning of quantum potentials and their essential relationships with the fundamental principles of quantum mechanics,

potential $\varphi_W(\boldsymbol{r}) = \varphi_b(\boldsymbol{r})$ on the one hand and potentials $\varphi_P(\boldsymbol{r})$ and $\varphi_f(\boldsymbol{r})$ on the other can be utilized in bonding analysis as functions for the localization of electrons and the revealing and description of electron lone pairs, respectively.

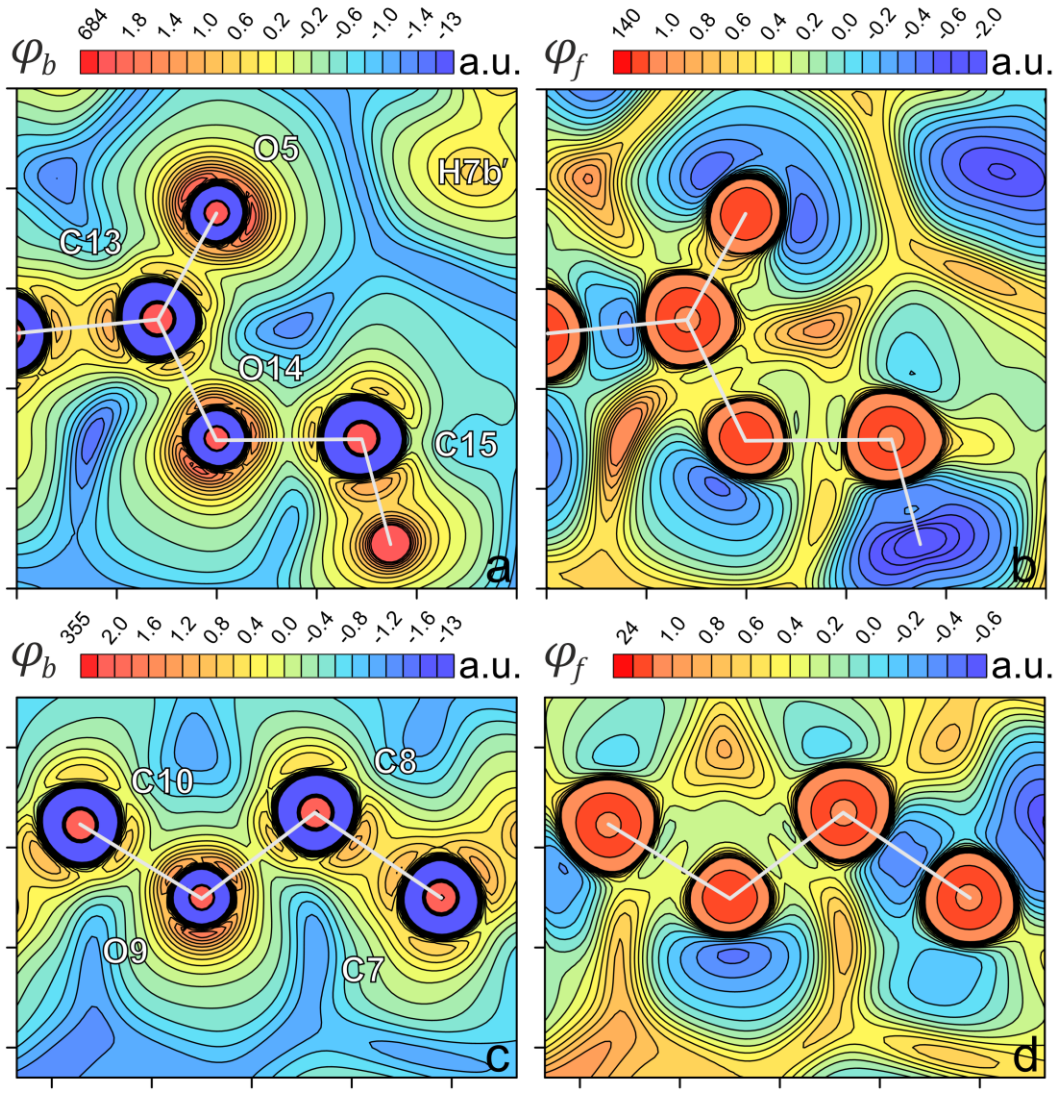

Figure 4. Distributions of bosonic $\varphi_b(\boldsymbol{r})$ (a, c) and fermionic $\varphi_f(\boldsymbol{r})$ (b, d) quantum potentials for the ester (a, b) and ether (c, d) functional groups of *ica* in the planes of labeled atoms. Contour steps are equal to 0.2 and 0.1 a.u. for $\varphi_b(\boldsymbol{r})$ and $\varphi_f(\boldsymbol{r})$, respectively. For the $\varphi_f(\boldsymbol{r})$ maps, additional contour at 8 a.u. is drawn to reveal the atomic shell structure. The maximum and

minimum function values are also given at the gradient scale bar. The distance between ticks on the graph axes is equal to 1 Å.

Simultaneous superposing atomic ρ- and atomic-like potential-based φ_{es}- and φ_k-basins offers a unique perspective on interatomic interactions and bonding within molecules and crystals.[15] The most important advantage of this approach is the clear visualization of gaps between boundaries of different types of ρ- and φ-basins apparent due to the natural differences in their shapes and volumes. The superpositions of φ_{es}- and φ_k-basins in the planes of selected functional groups of the *ica* molecule are shown as experimental gradient trajectories in Figure 5. In other words, curves on the figure are lines of ED gradient (gray), kinetic force (orange), and electric (blue) inner-crystal vector fields. Interestingly, the lines of different fields are intricately interwoven and intersect foreign zero-flux surfaces (bold lines), especially in the aforementioned gaps. The common characteristic of all the presented covalent bonds is the obligatory presence of saddle CPs (3, –1) in $\rho(\boldsymbol{r})$, $\varphi_k(\boldsymbol{r})$, and $\varphi_{es}(\boldsymbol{r})$ and corresponding gradient paths emerged at these points and following along similar trajectories between the nuclei of bonded atoms, that is not always the case for noncovalent ones. The immediate difference can be noted between polar and nonpolar covalent bonds. For the latter, such as C7–C8 (Figure 5d), all three CPs (3, –1) are located in exactly the same place and the corresponding ρ- and φ-basins' boundaries between the atoms coincide, manifesting the absence of total electron transfer. Conversely, in the case of polar covalent bonds, the CP (3, –1) in $\rho(\boldsymbol{r})$ stands apart along the interatomic line closer to the more electropositive atom, while the Lagrange CPs (3, –1) in $\varphi_k(\boldsymbol{r})$ and $\varphi_{es}(\boldsymbol{r})$ are positioned almost at the same place closer to an electronegative atom, which forms the gap between the boundaries of ρ- and φ-basins. Above, we have already noted the comparable sequence of saddle CPs along a bond line from an electropositive atom to an electronegative one as follows: CP (3, –1) in $\rho(\boldsymbol{r})$,

CP (3, +1) in $\varphi_{em}(\boldsymbol{r})$, and CP (3, –1) in $\varphi_{es}(\boldsymbol{r})$, with two latter very close to each other. In the vicinity of CPs (3, –1) in the potentials and ED, both atomic and φ-boundaries are generally nearly flat, which indicates an even action of the oppositely directed forces $\boldsymbol{F}_{es}(\boldsymbol{r})$ and $\boldsymbol{F}_{k}(\boldsymbol{r})$ normally to the ρ-boundary along the covalent bond line. Again, the electronic forces $\boldsymbol{F}_{es}(\boldsymbol{r})$ and $\boldsymbol{F}_{k}(\boldsymbol{r})$ act toward and away from the position of atomic nuclei within φ_{es}- and φ_{k}-basins, respectively. The forces $\mathcal{F}(\boldsymbol{r})$ and $\boldsymbol{F}_{k}(\boldsymbol{r})$ fully compensate each other.

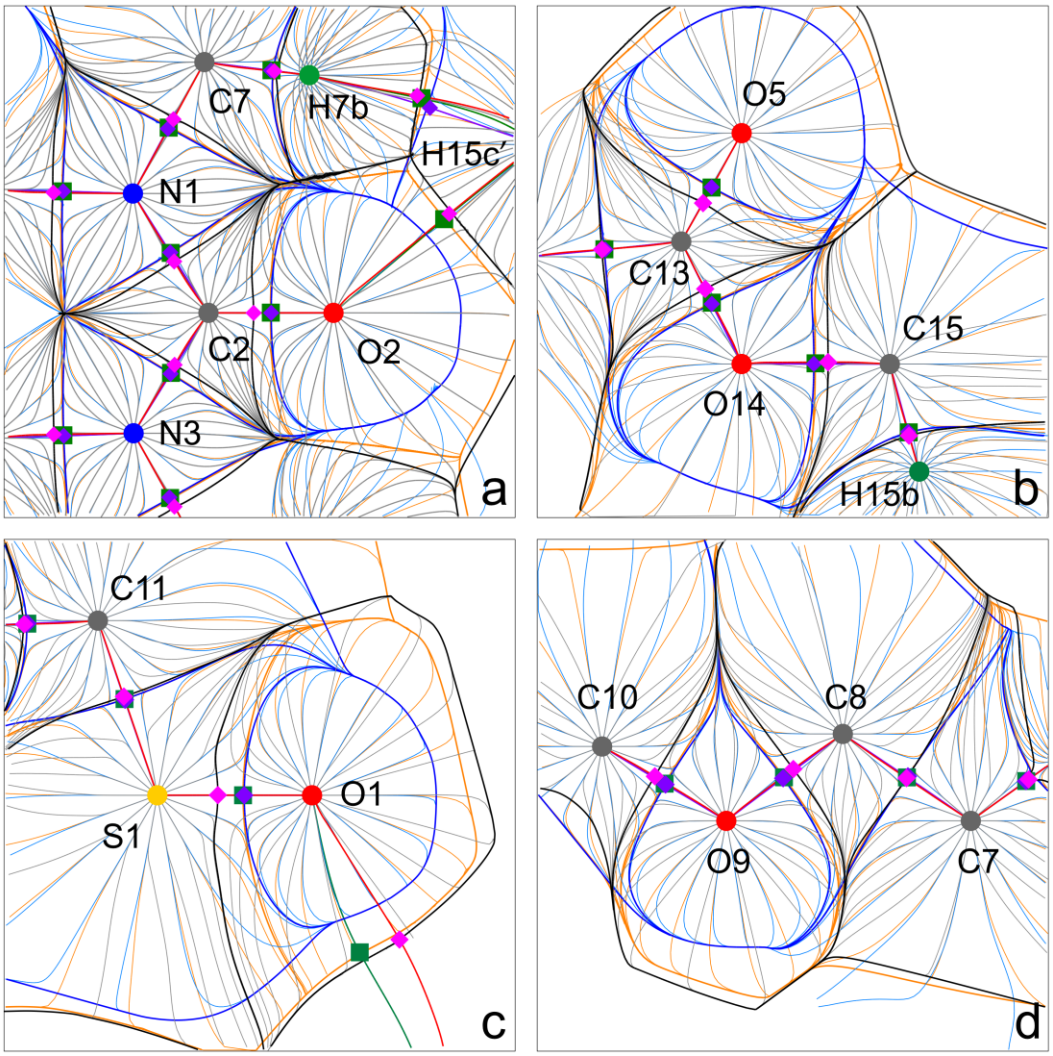

Figure 5. Superposition of gradient fields of electron density $\nabla\rho(\boldsymbol{r})$ (grey), electrostatic potential $\nabla\varphi_{es}(\boldsymbol{r})$ (blue), and kinetic potential $\nabla\varphi_{k}(\boldsymbol{r})$ (orange) calculated for the *ica* crystal in the planes

of labeled atoms. Saddle CPs (3, –1) in $\rho(\boldsymbol{r})$, $\varphi_{es}(\boldsymbol{r})$, and $\varphi_{k}(\boldsymbol{r})$ are shown by magenta and violet rhombuses and green squares, while gradient paths connecting the corresponding field attractors are shown by red, violet, and green lines, respectively. An extended version of the map (b) is shown in Figure S5. For H15c′···O2 (a), CP (3, –1) in $\varphi_{es}(\boldsymbol{r})$ is present but located out of the plane.

Keeping in mind that φ_{es}-basins behave as electrostatically isolated pseudoatomic regions and φ_{es}-boundaries play the role of envelopes of electric field lines, the observed gap between the boundaries of ρ- and φ_{es}-basins allows one to qualitatively describe the direction and extent of charge transfer between any two atoms, regardless of whether there is a bond path between the atoms or not.[15] ED held inside the volumetric gap between a QTAIM atom and an adjoining electric field pseudoatom belongs to this ρ-atom but experiences attractive $\boldsymbol{F}_{es}(\boldsymbol{r})$ toward the neighboring nucleus enclosed by the φ_{es}-basin. The ρ-basin of a more electronegative atom captures a portion of electrons of the neighboring φ_{es}-basin of an electropositive atom. As per the previously adopted terminology, an atom with a ρ-basin boundary extending further from its nucleus than its φ_{es}-basin boundary behaves as an electron occupier (e-occupier), and its connected neighbor behaves as an electron contributor (e-contributor). We deliberately avoid the frequently used terms like donor and acceptor when describing charge transfer, which may be misunderstood due to their vague usage for different cases, e.g., H-bond acceptor, electron-pair donor, etc. As can be seen from Figure 5, for the more polar covalent bonds, such as C=O and S=O, the gaps between the ρ- and φ_{es}-boundaries are wider than for the less polar ones, such as C–N bond. In our case, in the C=O, C–O, S=O, and C–N bonds, the oxygen and nitrogen atoms act as e-occupiers, while the carbon and sulfur ones as e-contributors. Notably, almost no visible gap between the ρ- and φ-boundaries can be found for the heteroatomic C–S covalent bond, since

these two elements have identical values of atomic electronegativity in the Mulliken scale of 6.22 eV. Similar considerations are valid for C–H bonds.

Similarly to the charge transfer described via the gap between the ρ- and φ_{es}-basin, the ρ-basin of an e-occupier atom captures a portion of the kinetic potential-based φ_k-basin of an e-contributor (Figure 5). For the covalent bonds, the φ_k-boundary always turns out to be very close to the φ_{es}-one, which is not inherent to other types of chemical interactions. Moreover, φ_k-boundary never moves beyond the φ_{es}-basin of an e-occupier atom. To the best of our knowledge, this observation has not been made before. While the gap between the boundaries of ρ- and φ_{es}-basins along the interatomic line can be interpreted as a real-space manifestation of the interatomic charge transfer, the gap between the ρ- and φ_k-boundaries corresponds to a different, yet unnamed phenomenon (see the Discussion section), which in the case of covalent bonds is carried out for virtually all transferred electrons contained within the ρ- and φ_{es}-gap. In general, this phenomenon is expected to be a part of electron transfer defined by the electric field but should be also associated with kinetic and exchange quantum effects. The latter becomes clear if one recalls that the shift of a CP (3, +1) in PAEM, and hence a CP (3, –1) in $\varphi_k(\boldsymbol{r})$, with respect to a CP (3, –1) in $\varphi_{es}(\boldsymbol{r})$ is governed by the $\varphi_x(\boldsymbol{r})$ contribution.

Hydrogen bonds and noncovalent interactions: kinetic and static potentials' aspects

Let us analyze the local one-electron potentials along the bond paths of the selected noncovalent interactions. Figure 6 features the one-dimensional profiles of the potentials for the nonclassical H12b···O9 (R_{ij} = 2.324 Å, E_g = 2.92 kcal mol^{-1}) and classical H1···O3 (R_{ij} = 1.425 Å, E_g = 15.75 kcal mol^{-1}) hydrogen bonds as well as very weak head-to-head sulfonyl interaction S1=O1···O1′=S1′ (R_{ij} = 3.339 Å, $E_g \approx$ 0.73 kcal mol^{-1}). For the weak intramolecular hydrogen

bond H12b···O9 and intermolecular interaction O1···O1′ from the *ica* crystal, distribution of $-\varphi_{es}(\boldsymbol{r})$ in the interatomic region away from the nuclei features a flat, linear plateau of near-zero potential values, which indicates that the $\varphi_{em}(\boldsymbol{r})$ distribution in the vicinity of BCPs is governed almost by $\varphi_{x}(\boldsymbol{r})$ contribution. This is not the case for the strongest hydrogen bond H1···O3 from oxalic acid dihydrate, for which the φ_{es}-barrier is significantly lower, with the maximum $-\varphi_{es}(\boldsymbol{r})$ value equal to ca. –0.21 a.u. Consequently, this H-bond has the comparably lowest PAEM barrier of approximately –0.87 a.u., while for the other presented noncovalent interactions it ranges –0.24 and –0.10 a.u. For the sake of comparison, covalent bonds displayed noticeably lower PAEM barriers, ranging from –2.2 to –1.0 a.u. (Figure 2). For both abovementioned H-bonds, the maximum of $\varphi_{em}(\boldsymbol{r})$ is significantly shifted from the corresponding BCP toward the oxygen atom (e-occupiers), while the maximum of $-\varphi_{es}(\boldsymbol{r})$ are located even deeper. For example, in the case of H1···O3 bond, the maxima of $\varphi_{em}(\boldsymbol{r})$ and $\varphi_{es}(\boldsymbol{r})$ are shifted ca. 0.14 and 0.18 Å away from the BCP toward the atom O3. By considering the slope of the $\varphi_{es}(\boldsymbol{r})$ and $\varphi_{em}(\boldsymbol{r})$ curves one can estimate the magnitude of corresponding forces $\boldsymbol{F}_{es}(\boldsymbol{r})$ and $\mathcal{F}(\boldsymbol{r})$ within the interatomic region.[15,84] For the noncovalent interactions, the magnitude of $\mathcal{F}(\boldsymbol{r})$ is generally higher than that of $\boldsymbol{F}_{es}(\boldsymbol{r})$, which is due to the more uneven distribution of $\varphi_{x}(\boldsymbol{r})$ along the bond paths. Further, the asymmetry of $\varphi_{em}(\boldsymbol{r})$ distribution is highly influenced by the $\varphi_{x}(\boldsymbol{r})$, which increases the steepness of the PAEM curve from the side of an e-occupier, in our cases the oxygen atom, and highly decreases the height of the φ_{em}-barrier for the whole interatomic region (see Figure 6c). On the other hand, the steeper curve from the side of an e-occupier indicates a higher degree of repulsion of electrons by the inner electric field, which is applicable to any kind of interaction. The shapes of $\varphi_{x}(\boldsymbol{r})$ and $\varphi_{em}(\boldsymbol{r})$ profiles along interatomic lines of various hydrogen bonds in optimized dimers has been recently discussed.[85]

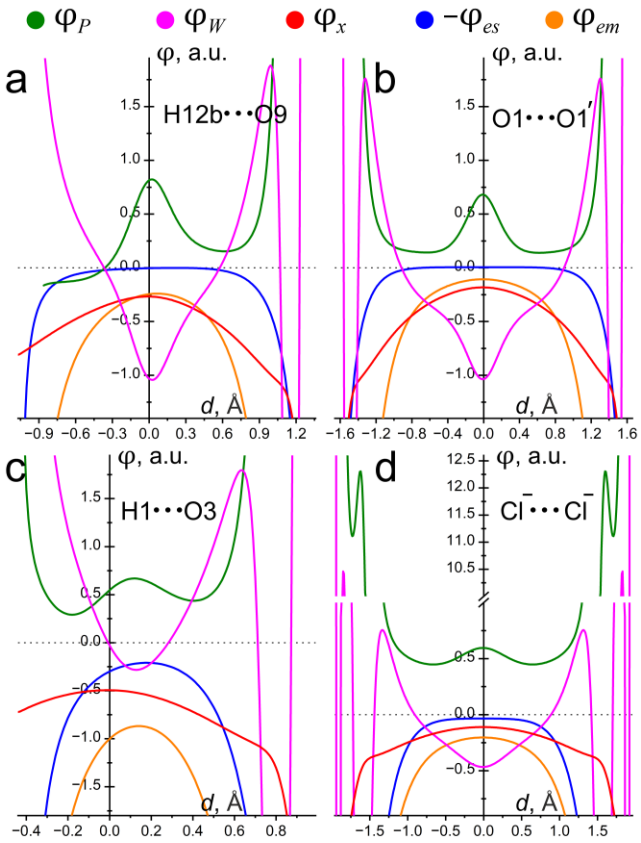

Figure 6. Behavior of Pauli $\varphi_P(\boldsymbol{r})$ (green), von Weizsäcker $\varphi_W(\boldsymbol{r})$ (magenta), exchange $\varphi_x(\boldsymbol{r})$ (red), and electronic electrostatic $-\varphi_{es}(\boldsymbol{r})$ (blue) potentials and static potential acting on an electron in a molecule $\varphi_{em}(\boldsymbol{r})$ (orange) along the bond paths of the selected noncovalent interactions in the *ica* (a, b), oxalic acid dihydrate (c), and sodium chloride (d) crystals. Zero value on the *x*-axes corresponds to the position of corresponding BCPs.

The other notable difference between covalent and noncovalent bonds lies in the distribution of von Weizsäcker $\varphi_W(\boldsymbol{r})$ and Pauli $\varphi_P(\boldsymbol{r})$ potentials. Instead of the continuous region of positive $\varphi_W(\boldsymbol{r})$ in the middle of bonds, which correspond to allowed positive values of the local one-electron kinetic energy, we observe a sharp and wide negative potential peak (von Weizsäcker well), which indicates a region of electron depletion where $\boldsymbol{F}_W(\boldsymbol{r})$ attempts to drag the electrons, but classical electron motion is forbidden and electrons exhibit the quantum behavior. For instance,

both nonclassical H12b···O9 and classical H1···O3 hydrogen bonds feature deep and shallow negative von Weizsäcker wells with the potential minima of ca. –1.04 and –0.28 a.u., respectively, (Figure 6a,c). A series of positive peaks of $\varphi_W(\boldsymbol{r})$ located closer to the nuclei of oxygen atoms corresponds to the lone (but involved in the interaction) electron pair ED concentration within the L atomic shell and the ED within the K electron shell. Similarly, for the homoatomic Cl···Cl interaction found in the NaCl crystal (Figure 6d), the profile of $\varphi_W(\boldsymbol{r})$ features the negative von Weizsäcker well (φ_W(BCP) = –0.47 a.u.) and three consecutive peaks with increasing values for each Cl^- anion, which in turn correspond to the atomic M, L, and K electron shells. Turning to the one-dimensional distributions of $\varphi_P(\boldsymbol{r})$ along the bond paths of the noncovalent interactions, the immediate difference between covalent and noncovalent bonds is the absence of a flat, linear section of near-zero Pauli potential. Instead, for these interactions there exist a pronounced Pauli barrier, i.e., a local maximum of $\varphi_P(\boldsymbol{r})$ in the interatomic region separating the two atoms.[15] Height of a Pauli barrier therefore reflects the extent of Pauli repulsion occurring between same-spin electrons in the interatomic region due to the lack of sharing interaction. In turn, $\boldsymbol{F}_P(\boldsymbol{r})$ acts on electrons pushing them away from the barrier in the directions of the respective potential minima into their atomic basins. Notably, Pauli barriers accompany negative von Weizsäcker wells. Figure 6 illustrates the difference in the height of Pauli barriers for the studied interactions: the local maximum of $\varphi_P(\boldsymbol{r})$ reaches ca. 0.82 a.u for the weaker H-bond H12b···O9, while for the stronger H1···O3 bond it has a lower value of ca. 0.67 a.u. For the two considered hydrogen bonds, the Pauli barrier and the von Weizsäcker well are shifted closer to the oxygen atoms. In the case of two noncovalent homoatomic interactions (Figure 6b,d), one can notice that the distribution of $\varphi_P(\boldsymbol{r})$ for the O1···O1′ one has a tall, rather narrow positive potential peak with a maximum at ca. 0.68 a.u., while for the Cl^-···Cl^- one the maximum of ca. 0.59 a.u. lies at the top of a short, quite

broad peak. It might be however more useful to consider the relative height of the Pauli barrier, i.e., the potential difference between neighboring maxima and minima of $\varphi_P(\boldsymbol{r})$. For O1···O1′, the Pauli barrier has a height of ca. 0.54 a.u., while for $Cl^-\cdots Cl^-$ it reaches at most 0.14 a.u. Judging by this difference, one can assume that the latter interaction involves a greater contribution of ED sharing between the two atoms. This conclusion is also supported by the lower PAEM barrier for $Cl^-\cdots Cl^-$ as compared to O1···O1′ (–0.20 a.u. versus –0.10 a.u.).

As has been shown previously, the most suitable and reasonable way to define the molecular surface in crystals for subsequent analysis of various properties on it is to choose the outer boundaries of ρ-basins.[15,63,86] Figure 7 features the ρ-basins constructed for *ica* in the crystal with $-\varphi_{es}(\boldsymbol{r})$ and $\varphi_{em}(\boldsymbol{r})$ mapped on them, which represent another view on performance of φ_{es}- and φ_{em}-barriers. Analogous maps for oxalic acid dihydrate, sodium chloride, and magnesium diboride are presented in Figure S6. Within the regions centered around the BCPs, a local increase or decrease of $\varphi_{es}(\boldsymbol{r})$ can be detected. PAEM $\varphi_{em}(\boldsymbol{r})$ is likely a more suitable function for the identification and characterization of interatomic interactions, since it explicitly accounts for static electron exchange. In practice, $\varphi_{em}(\boldsymbol{r})$ is negative everywhere, and the enclosed areas with more negative values of $\varphi_{em}(\boldsymbol{r})$ are observed near the BCPs, which help recognize diverse chemical interactions (Figure 7b). On the ρ-boundaries, $\mathcal{F}(\boldsymbol{r})$ acts in the direction of reducing $\varphi_{em}(\boldsymbol{r})$, i.e., nearby the BCPs, thus promoting their formation.[15]

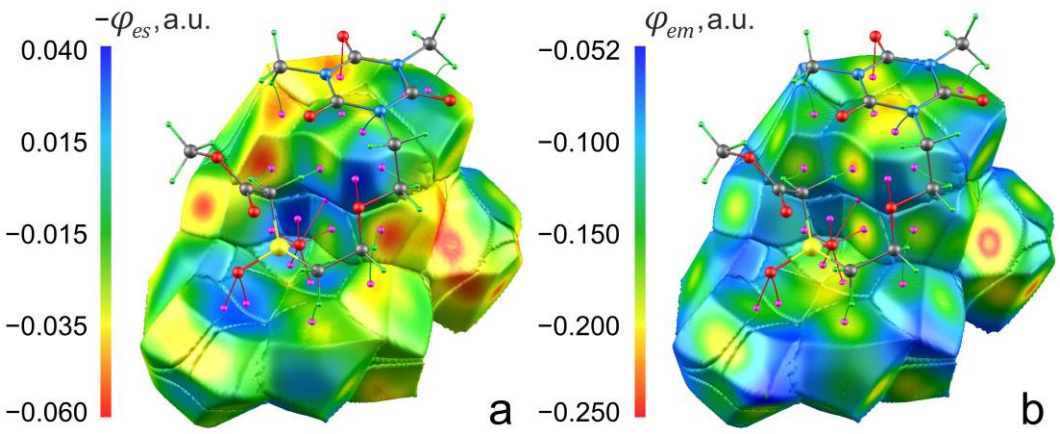

Figure 7. Inner-crystal electronic electrostatic potential $-\varphi_{es}(\boldsymbol{r})$ (a) and static potential acting on an electron in a molecule $\varphi_{em}(\boldsymbol{r})$ (b) mapped on the surfaces of ρ-basins for *ica* in the crystal. BCPs and bond paths for the noncovalent interactions with the neighboring molecule related by the inversion center are presented as magenta spheres and multicolored lines.

Figure 8 displays the bosonic $\varphi_b(\boldsymbol{r})$ and fermionic $\varphi_f(\boldsymbol{r})$ quantum potentials in the plane of oxalic acid containing three different classical hydrogen bonds with the water molecules. For the atoms O1 and O2, lone electron pairs identified by the regions of highly positive $\varphi_b(\boldsymbol{r})$ and negative $\varphi_f(\boldsymbol{r})$ are directed toward the ED depletion regions of the neighboring hydrogen atoms. Both oxygen atoms hence act as a donor of the lone pair, being at the same time an e-occupier (vide infra), while the hydrogen atoms are simultaneously an acceptor and e-contributor. For each of the hydrogen bonds H1···O3, H3′···O2, and H2″···O2, a local increase of $\varphi_b(\boldsymbol{r})$ and a corresponding decrease of $\varphi_f(\boldsymbol{r})$ in the interatomic region are observed, which form the channels somewhere along the bond path within the respective potential distributions. For comparison, Figure S7 shows similar contour maps for the O···O contact in the *ica* crystal, from which it is obvious that the VSCCs of oxygen atoms are directed directly at each other, thereby indicating a surface-to-surface way of molecular recognition. Thus, $\varphi_b(\boldsymbol{r})$ and $\varphi_f(\boldsymbol{r})$ can reveal noncovalent

interactions and further distinguish between the Lewis (donor-acceptor or "key-lock") and van der Waals (surface-to-surface) mechanism of interactions. A more unique observation can be made regarding the representation of electron lone pairs in the $\varphi_b(\boldsymbol{r})$ and $\varphi_f(\boldsymbol{r})$ distributions. In the interatomic region of the strongest H-bond H1···O3, the lone electron pair of the oxygen atom O3 is well localized in $\varphi_b(\boldsymbol{r})$ showing the nonbonding VSCC lobe directed to H1 qualitatively and quantitatively similar to the other nonbonding VSCCs (Figure 8a). However, in the $\varphi_f(\boldsymbol{r})$ distribution, the same lone electron pair presents highly distorted, most likely because a significant portion of the transferred ED is shared with the neighboring H1 atom under the influence of electron exchange effects. We believe that complementary analysis of the $\varphi_f(\boldsymbol{r})$ and $\varphi_P(\boldsymbol{r})$ distribution can be further exploited to gain some insights into ED sharing within donor-acceptor bonding. The theoretical maps of electronic potentials and various popular functions in the plane of the oxalic acid molecule are present in Figure S8.

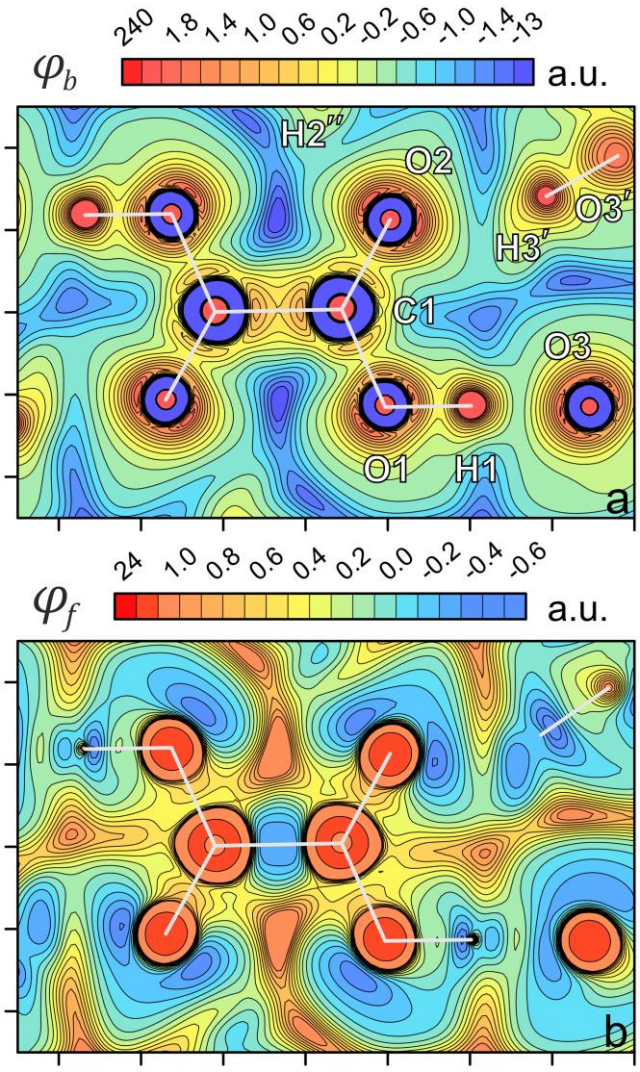

Figure 8. Contour maps of bosonic $\varphi_b(\boldsymbol{r})$ (a) and fermionic $\varphi_f(\boldsymbol{r})$ (b) quantum potentials for the oxalic acid dihydrate crystal. Contour steps are equal to 0.2 and 0.1 a.u. for $\varphi_b(\boldsymbol{r})$ and $\varphi_f(\boldsymbol{r})$, respectively. For the $\varphi_f(\boldsymbol{r})$ map (b), additional contour at 8 a.u. is drawn to reveal the atomic shell structure. The maximum and minimum function values are also given at the gradient scale bar. The distance between ticks on the graph axes is equal to 1 Å.

As we noted above, the width of the gaps between boundaries of ρ- and φ-basins vary significantly within and outside the molecule in a crystal. The superpositions of ρ-, φ_{es}-, and φ_k-basins in the planes of various intermolecular interactions in the crystals of *ica* and oxalic acid

dihydrate are shown as gradient trajectories in Figures 5a and 9. As opposed to covalent bonds, for noncovalent interactions, not all three expected CPs (3, –1) in $\rho(\boldsymbol{r})$, $\varphi_{es}(\boldsymbol{r})$, and $\varphi_k(\boldsymbol{r})$ and associated ρ- and φ-paths may be present. Even if all these CPs are present, the corresponding paths do not always follow the same trajectory. A quite intriguing picture is observed for the intramolecular sulfonyl-ether O1···O9 (R_{ij} = 3.275 Å, $E_g \approx 0.81$ kcal mol^{-1}) and centrosymmetric intermolecular sulfonyl-sulfonyl O1···O1′ interactions in the *ica* crystal shown in Figure 9a,b. For both interactions, no common φ_{es}-basin boundary between the bonded oxygen atoms is present and, consequently, the CPs (3, –1) and corresponding path in $\varphi_{es}(\boldsymbol{r})$ do not exist. Further, for both interactions, the common φ_k-boundary between the contacting oxygen atoms exists. This boundary almost coincides with the ρ-one, but is not, however, accompanied by the corresponding gradient φ_k-path.

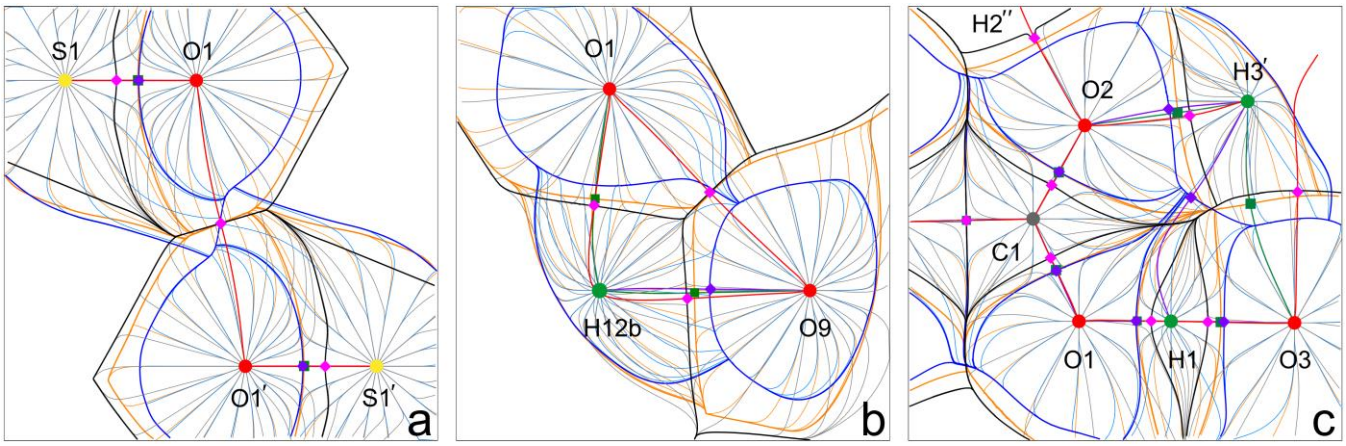

Figure 9. Superposition of gradient fields of electron density $\nabla\rho(\boldsymbol{r})$ (grey), electrostatic potential $\nabla\varphi_{es}(\boldsymbol{r})$ (blue), and kinetic potential $\nabla\varphi_k(\boldsymbol{r})$ in the *ica* (a, b) and oxalic acid dihydrate (c) crystals in the planes of labeled atoms. Saddle CPs (3, –1) in $\rho(\boldsymbol{r})$, $\varphi_{es}(\boldsymbol{r})$, and $\varphi_k(\boldsymbol{r})$ are shown by magenta and violet rhombuses and green squares, while gradient paths connecting corresponding

field attractors are shown by red, violet, and green lines, respectively. For H2″···O2 (c), CPs (3, –1) in $\varphi_{es}(\boldsymbol{r})$ and $\varphi_{k}(\boldsymbol{r})$ are present but located out of the plane.

For the centrosymmetric S1=O1···O1′=S1′ interaction, the superposition of atomic and potential basins helps uncover an electrostatic contribution to the bond formation. Recall that this closed-shell interaction refers to the van der Waals type. Although there is no common φ_{es}-boundary between the two oxygen atoms, it is unexpectedly present between the two sulfur atoms as well as between the oxygen and sulfur atoms of the two neighboring sulfonyl groups (Figure 9a). So, the ρ-basin of O1 captures a portion of electrons contained in the φ_{es}-basin of S1′. From this we can conclude that each oxygen atom in this interaction acts as an e-occupier with respect to the sulfur atom of the neighboring molecule, identifying the electrostatic interaction between pairs of nonbonded atoms O1 and S1′ as well as O1′ and S1 within the topologically bonded O1···O1′ contact. This observation is the real-space evidence of the direct influence of surrounding atoms on the interaction. Therefore, the proposed approach of basin superposition helps reveal the actual mechanism of bond formation, which could not be extracted by the standard topological analysis of ED alone.

A special mention needs to be given to CP (3, –1) in $\varphi_{es}(\boldsymbol{r})$ between the two hydrogen atoms H1 and H3′, which share a common φ_{es}-boundary not mirrored in either $\rho(\boldsymbol{r})$ or $\varphi_{k}(\boldsymbol{r})$. Conversely, between O3 and H3′ there is only CP (3, –1) in $\varphi_{k}(\boldsymbol{r})$, although all three common boundaries are present. Even though the oxygen atom O3 acts as an electron occupier with respect to the hydrogen atom H3′, while the bond path goes between the two oxygen atoms O3 and O3′ (Figure 9c).

The use of gradient fields superposition can also help distinguish between weak and moderately strong hydrogen bonds. Let us consider a number of hydrogen bonds, which include

the nonclassical H12b···O9 (R_{ij} = 2.324 Å, ρ(BCP) = 0.087 e Å^{-3}, $\nabla^2\rho$(BCP) = 1.27 e Å^{-5}, E_g = 2.92 kcal mol^{-1}) and H12b···O1 (R_{ij} = 2.426 Å, ρ(BCP) = 0.058 e Å^{-3}, $\nabla^2\rho$(BCP) = 0.88 e Å^{-5}, E_g = 1.93 kcal mol^{-1}) ones from the *ica* crystal (Figure 9b) as well as the three classical hydrogen bonds H1···O3 (R_{ij} = 1.425 Å, ρ(BCP) = 0.657 e Å^{-3}, $\nabla^2\rho$(BCP) = –0.11 e Å^{-5}, g(BCP) = 5.85·10^{-2} a.u., v(BCP) = –1.18·10^{-1} a.u., E_g = 15.75 kcal mol^{-1}), H2″···O2 (R_{ij} = 1.852 Å, ρ(BCP) = 0.230 e Å^{-3}, $\nabla^2\rho$(BCP) = 1.50 e Å^{-5}, E_g = 5.55 kcal mol^{-1}), and H3′···O2 (R_{ij} = 1.903 Å, ρ(BCP) = 0.194 e Å^{-3}, $\nabla^2\rho$(BCP) = 1.59 e Å^{-5}, E_g = 5.05 kcal mol^{-1}) from the oxalic acid dihydrate crystal (Figure 9c). For all the H-bonds, the ρ-basins of the oxygen atoms always occupy a part of the φ_{es}- and φ_k-basins of the contacting hydrogen atoms, so that there exists a gap between the zero-flux surfaces of the corresponding ρ- and φ-basins. Therefore, the oxygen atoms always act as an e-occupier, while the hydrogen atoms are e-contributors. Recall that the penetration of ρ- and φ_{es}-basins represents electron transfer defined by the electric field, while the penetration of ρ- and φ_k-basins corresponds to the unnamed quantum phenomenon (vide supra) defined by the kinetic and static force fields, which is a part of charge transfer. We noted that the φ_k-boundary does not move beyond the φ_{es}-basin of the oxygen atoms and changes its position between the ρ- and φ_{es}-ones depending on the actual nature and strength of the H-bond in question. For the weaker H-bonds H12b···O9 and H12b···O1, the φ_k-boundary is located closer to the ρ-one, while, for the stronger H-bonds H2″···O2 and H3′···O2, it appears closer to the φ_{es}-boundary. A special case is the strongest hydrogen bond H1···O3, for which the φ_k-boundary closely approaches the φ_{es}-one, so that the arrangement of atomic and potential basin boundaries begins to closely resemble a very polar covalent bond (compare with O1–H1). At the same time, a noticeable gap between the φ_{es}- and φ_k-boundaries is still present not only on the periphery but also along the ρ- and φ-paths. In other words, a stronger hydrogen bond is accompanied by the deeper penetration of hydrogen's

φ_k-pseudoatom into oxygen's ρ-atom, so that the φ_{es}- and φ_k-basins of the hydrogen atom occupy almost the same region of space. Conversely, for the weaker hydrogen bonds, only hydrogen's electric field pseudoatom (φ_{es}-basin) is able to deeply penetrate the ρ-basin of the oxygen atom. Comparing the magnitude of one-electron $\boldsymbol{F}_k(\boldsymbol{r})$ acting on the zero-flux surface at the position of the BCP for the three classical hydrogen bonds, the highest value of ca. 2.0 a.u. is observed for the strongest H1···O3 bond, while for the weaker H2″···O2 and H3′···O2 bonds the corresponding values are equal to 0.66 and 0.63 a.u. This reasoning can be carried over to any other interactions. However, the extent of penetration of e-contributing atom's φ_k-basin into the ρ-basin of e-occupier is not actually directly tied with bond strength, rather it shows the degree of apparent covalency of an interaction. In our previous work, we noted that the two strongest noncovalent interactions in the crystal of a uracil derivative, which are the C=O···π and C(*sp*)–H···O contacts, have similar estimated bond energies E_g.[15] However, for the former contact, the φ_k-boundary is located very close to the ρ-one indicating the dominating electrostatic contribution, while for the latter it appears between the φ_{es}- and ρ-basin boundaries alluding to the large "covalent component". A more general conclusion regarding the chemical meaning of mutual arrangement of atomic and potential basins will be made in the Discussion.

From the topological characteristics for H1···O3, i.e., the negative values of $\nabla^2\rho(\mathrm{BCP})$ and total electronic energy density at the BCP as well as the ratio $|v(\mathrm{BCP})|/g(\mathrm{BCP}) > 2$,[83] one might assume that this interaction can be formally categorized as a shared one. Our data match the previous experimental charge density study of oxalic acid dihydrate.[87] However, such conclusion is most likely not true, since the value of $\rho(\mathrm{BCP})$ is relatively small and $\nabla^2\rho(\mathrm{BCP})$, although negative, is very close to zero. Additionally, Laplacian of ED suffers from the model quality and has a large experimental error.[88] Topological analysis performed directly using the periodic

wavefunction (ωB97X/pob-TZVP-rev2) yields the relatively small ρ(BCP) = 0.610 e Å^{-3}, while the value of $\nabla^2\rho$(BCP) is positive and equal to 3.016 e Å^{-5}. To avoid the false categorization, we compare the gradient fields' behavior for the H1···O3 hydrogen bond and neighboring covalent bond O1–H1 (Figure 9c). Immediately, a clear distinction is noticed: for the covalent bond O1–H1, although undoubtedly highly polar in nature, the boundaries of φ_{es}- and φ_k-basins almost coincide diverging to some extent at the periphery, which is characteristic of covalent bonds, while the hydrogen bond H1···O3 exhibits a clear gap between the two zero-flux surfaces of potential-based basins.

Closed shell interactions in ionic crystals

Now we can turn our attention to the ionic crystals of sodium chloride and magnesium diboride. The distributions of various potentials along the bond paths of Na···Cl and Mg···B are featured in Figure 10 and resemble noncovalent interactions in molecular crystals. The shape of the $\varphi_x(\boldsymbol{r})$ graphs in the middle of the bond lines features the linear segment significantly skewed in the direction of the anions. The profiles of static potentials $\varphi_{em}(\boldsymbol{r})$ and $-\varphi_{es}(\boldsymbol{r})$ demonstrate significant asymmetry. Maxima of both $\varphi_{em}(\boldsymbol{r})$ and $-\varphi_{es}(\boldsymbol{r})$ are noticeably shifted from the BCP toward the respective anion, while the potential graphs retain a somewhat parabolic shape. The maximum of the PAEM barriers is ca. –0.35 a.u. for Na···Cl and ca. –0.61 a.u. for Mg···B. In the case of NaCl, a shift of $\varphi_{em}(\boldsymbol{r})$ relative to $-\varphi_{es}(\boldsymbol{r})$ is especially noticeable and equal to about 0.14 Å. As before, the graphs of $\varphi_W(\boldsymbol{r})$ and $\varphi_P(\boldsymbol{r})$ highlight the atomic shell structure. However, the expected maxima and minima in these potentials for both Na and Mg atoms corresponding to the outermost atomic electron shells are missed due to the occurred valence electron transfer. For the ionic bonds Na···Cl and Mg···B, the deep negative von Weizsäcker well exists, with the

potential minimum values of –1.92 and –1.73 a.u., respectively. This well in turn is accompanied by the Pauli barrier, with maxima in $\varphi_P(\boldsymbol{r})$ of 2.28 and 2.60 a.u. Both von Weizsäcker well and Pauli barrier are located in the atomic basin of the Na^+ and Mg^{2+} cations. Conversely, within the atomic basins of Cl^- and B^- anions, the positive local maximum of $\varphi_W(\boldsymbol{r})$ and the wide local minimum of $\varphi_P(\boldsymbol{r})$ are observed, which correspond to the positions of paired valence ED localization. This pattern of $\varphi_W(\boldsymbol{r})$ and $\varphi_P(\boldsymbol{r})$ local extrema is consistent with the asymmetry of charge distribution expected for ionic bonds. A quite intriguing feature of the $\varphi_P(\boldsymbol{r})$ distribution is a small local minimum near the Pauli barrier within the cationic ρ-basin. This local minimum of $\varphi_P(\boldsymbol{r})$ is more pronounced for Na^+, while it practically merges with the Pauli barrier for Mg^{2+}. The possible explanation for this is almost complete charge transfer followed by effective electron pairing in the case of MgB_2, for which the cationic atom has a Bader charge of +1.92 e, i.e., very close to a formal charge of +2 e. This assumption is supported by the lower φ_{em}-barrier. Also noteworthy is the noticeable electrophilicity of the boron atom in compounds, as well as its pronounced ability to act as a Lewis acid. For NaCl, the total electron transfer between atoms is equal to ca. 0.82 e.

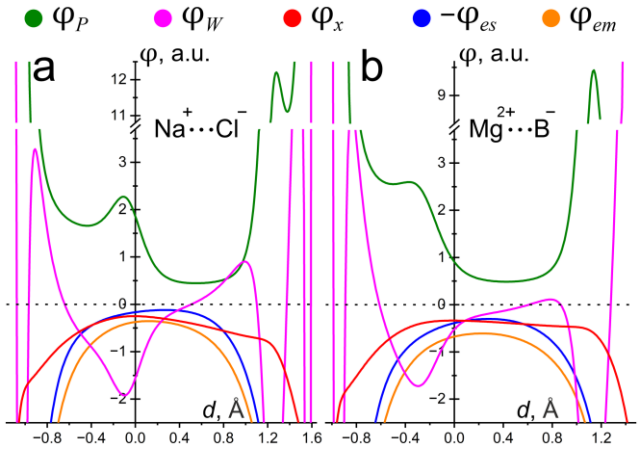

Figure 10. Behavior of Pauli $\varphi_P(\boldsymbol{r})$ (green), von Weizsäcker $\varphi_W(\boldsymbol{r})$ (magenta), static exchange $\varphi_x(\boldsymbol{r})$ (red), and inverted electrostatic $-\varphi_{es}(\boldsymbol{r})$ (blue) potentials and static potential acting on an electron in a molecule $\varphi_{em}(\boldsymbol{r})$ (orange) along the bond paths Na···Cl (a) and Mg···B (b) in sodium chloride and magnesium diboride. Zero value on the *x*-axes corresponds to the positions of corresponding BCPs. For the potential profiles along the bond paths of covalent B–B and noncovalent B···B interaction in the magnesium diboride crystal see Figure S9.

Contrary to the simplified chemical interpretation of bonding in ionic compounds, interacting ions can hardly be described as spherical and performing non-directional interactions. Moreover, their electron distribution reveals a quite pronounced and specific valence-shell structure. Let us now consider the behavior of quantum potentials $\varphi_b(\boldsymbol{r})$ and $\varphi_f(\boldsymbol{r})$ in the studied salts featured in Figures 11. Both cations in their outer regions feature deep minima and maxima of $\varphi_b(\boldsymbol{r})$ and $\varphi_f(\boldsymbol{r})$, respectively, indicating the electron depletion regions. Conversely, both anions in their outer regions feature deep maxima and minima of $\varphi_b(\boldsymbol{r})$ and $\varphi_f(\boldsymbol{r})$, respectively, indicating VSCCs or paired ED concentration arias. Around each Cl^- anion, lobes of locally enhanced $\varphi_b(\boldsymbol{r})$ or decreased $\varphi_f(\boldsymbol{r})$ potentials are directed at the respective regions of decreased $\varphi_b(\boldsymbol{r})$ and enhanced $\varphi_f(\boldsymbol{r})$ potentials at the Na^+ cation. In the case of NaCl, both pairs of positive and negative lobes exactly lie on the bond path trajectory. This bonding picture corresponds to the Lewis type of interaction between already formed Na^+ (acceptor) and Cl^- (donor) ions. The distribution of $\varphi_k(\boldsymbol{r})$ does not reveal any inner atomic structure. However, the channels of locally increased kinetic potential are formed along the bond lines, where $\varphi_k(\boldsymbol{r})$ reaches 0.28 a.u. for Na···Cl and 0.44 a.u. for Mg···B (Figure S10).

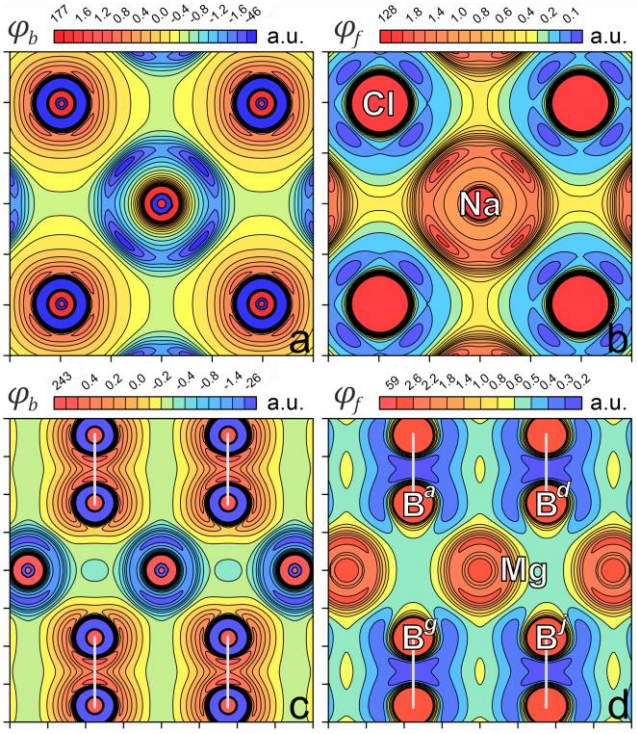

Figure 11. Distributions of bosonic $\varphi_b(\boldsymbol{r})$ (a, c) and fermionic $\varphi_f(\boldsymbol{r})$ (b, d) quantum potentials for the NaCl (top) and MgB_2 (bottom) crystals. For $\varphi_b(\boldsymbol{r})$ contour steps are equal to 0.2 a.u., while for $\varphi_f(\boldsymbol{r})$ a step of 0.1 a.u. is adopted in the function range between 0 and 1 a.u. and a step of 0.2 a.u. in the range from 1 to 2 a.u. The maximum and minimum function values are given at the gradient scale bar. For the orientation of the selected map plane for MgB_2 see Figure S11.

An interesting feature of the Mg···B interaction is that its bond path is significantly curved inwards in the direction of the crystallographic 6-fold rotation axis going through the Mg nucleus, as shown in Figures 12 and 13. Along each Mg···B bond path there exist channels of minimal exchange and correlation energy densities per electron, with the local maximum located at the BCP (Figure S12). This indicates some tension in the system. In the literature, there are several charge density studies of metal complexes, where curved bond paths involving metal atoms were found.[89–92] This observation was explained by the dominant contribution of back π-donation to the bonding

between a metal and an atom of a ligand as compared with direct σ-donation, which was deduced by means of the $\nabla^2\rho(\boldsymbol{r})$ distribution. However, in our case the analysis of $\nabla^2\rho(\boldsymbol{r})$ does not lead to a similar conclusion. An interpretation of the observed feature can be retrieved from the deformation ED $\delta\rho(\boldsymbol{r})$ (Figure 12b) supported by the $\varphi_b(\boldsymbol{r})$ and $\varphi_f(\boldsymbol{r})$ distribution. The atomic basin of the Mg^{2+} cation is elongated along the mentioned 6-fold rotation axis toward the centers of two six-membered boron rings (Figure 1g). Along this axis, two small lobes of positive $\delta\rho(\boldsymbol{r})$ can be located inside the manganese's ρ-basin, which indicate the regions of local ED accumulation. These are loosely directed at the ED reduction regions near the B^- anions. The bent Mg···B bond paths cross the regions of local electron accumulation near the Mg^{2+} ion and proceed through the narrow zone of ED reduction at the B^- anion, which serves as (Figure 12b) strong evidence of the existence of donor-acceptor interaction between counterions. Importantly, the valence region of Mg^{2+} ion appears to be fully deconcentrated, as indicated by the highly positive $\nabla^2\rho(\boldsymbol{r})$ values, however $\varphi_b(\boldsymbol{r})$ and $\varphi_f(\boldsymbol{r})$ allow one to detail this depleted region. It seems that the two small regions of electron accumulation and concentration at the Mg^{2+} cation correspond to local increase and decrease of $\varphi_b(\boldsymbol{r})$ and $\varphi_f(\boldsymbol{r})$ within very negative and positive areas, respectively (Figure 12a,c,d). The course of direct ED donation thus coincides with the way of charge transfer, so that Mg^{2+} simultaneously plays a role of an ED donor in terms of the $\delta\rho(\boldsymbol{r})$ distribution and an e-contributor in terms of mutual arrangement of ρ- and φ_{es}-basins (see below). On the other hand, the pronounced regions of ED accumulation and concentration near the B^- anions do exist, which are also reflected in the $\varphi_b(\boldsymbol{r})$ and $\varphi_f(\boldsymbol{r})$ maps. These in turn are directed toward the continuous toroidal belt of ED reduction and depletion within the outer shell of the Mg^{2+} ion as shown in Figure 12b-d (see Figure S13 for the 3D picture). Consequently, we observe the ED donation in a backward direction, i.e., from the charge accumulations and concentrations

at the B^- anions to the toroidal belt of charge reduction and depletion around the Mg^{2+} cation, which in fact is not supported by the bond path.

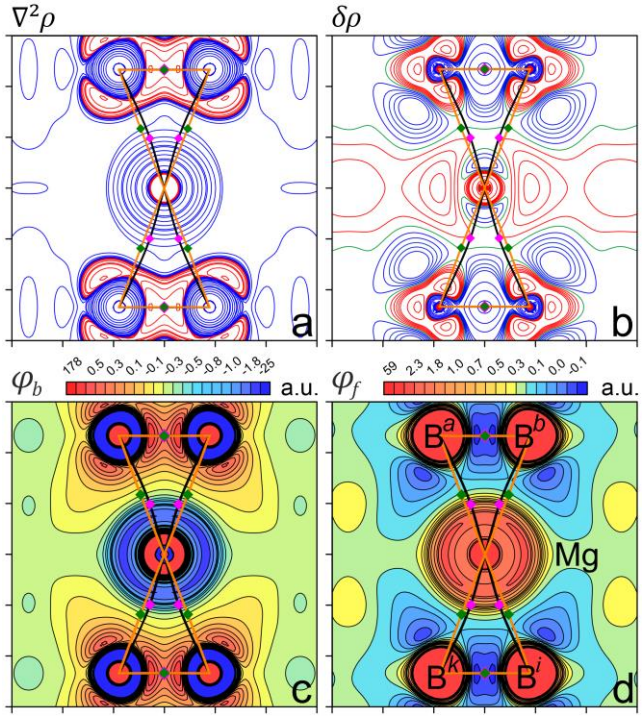

Figure 12. Distributions of the Laplacian of electron density $\nabla^2\rho(\boldsymbol{r})$ [e Å^{-5}] (a), deformation electron density $\delta\rho(\boldsymbol{r})$ [e Å^{-3}] (b), quantum bosonic potential $\varphi_b(\boldsymbol{r})$ (c), and quantum fermionic potential $\varphi_f(\boldsymbol{r})$ (d) showing the trajectories of ρ- and φ_k-paths between the Mg and B atoms. Distance between major ticks is equal to 1 Å. For (a), the logarithmic scale in the form of ±1, 2, 4, $8\cdot10^n$, n = (–2, –1, 0, 1, 2) is adopted. For (b), the contour step is equal to 0.05 e Å^{-3} in the whole function range and 0.01 between –0.05 and 0.05 e Å^{-3}. For the orientation of the selected map plane for MgB_2 see Figure S11.

The bond path Mg···B avoids crossing the lobes of $\varphi_b(\boldsymbol{r})$ and $\varphi_f(\boldsymbol{r})$, as would be expected at first sight. Nevertheless, as mentioned a few lines above, there exists the channel of locally enhanced $\varphi_k(\boldsymbol{r})$ between the topologically bonded Mg and B atoms, inside of which an almost

straight φ_k-path is formed (Figures 12 and 13). We believe that the subtle balance of the $\varphi_W(\boldsymbol{r})$ and $\varphi_P(\boldsymbol{r})$ potentials, which leads to the optimal distribution of the kinetic potential $\varphi_k(\boldsymbol{r}) = \varphi_W(\boldsymbol{r}) + \varphi_P(\boldsymbol{r})$, can also explain this intricate and any other interactions. This optimum is apparently expressed in the presence of a saddle CP (3, –1) in kinetic potential and φ_k-path between interacting atoms. Here we stress the importance of joint analysis of partial kinetic potentials as well as the kinetic force field $\boldsymbol{F}_k(\boldsymbol{r})$ to get a comprehensive picture of bonding in molecules and crystals.

To conclude our study of ionic compounds, let us analyze the superpositions of ρ- and φ-basins featured as experimental gradient trajectories in Figure 13. Both NaCl and MgB_2 follow the established trend of mutual arrangement of ρ- and φ-basins, displaying large, visible gaps between basin boundaries. Each potential-based basin of the Na or Mg metals expands into the corresponding 6 and 12 atomic basins of the surrounding Cl or B non-metals so that the portion of its space containing a certain amount of electron density appears inside the mentioned atomic basins. Following the direction of charge transfer, the Na and Mg atoms act as e-contributors to Cl and B atoms, respectively. As expected for ionic bonds, a substantial degree of charge transfer is reflected by the gaps between the boundaries of ρ- and φ_{es}-basins, which are noticeably wider than for the covalent bonds, reaching 0.28 Å in the case of NaCl and 0.29 Å in the case of MgB_2. Relatively simple crystalline structures of both compounds allow for a quantitative estimation of volumes for these gaps, which can be calculated as a difference between the volumes of ρ- and φ_{es}-basins divided by the number of bonds. Table S1 contains the volumes and charges for atomic and potential basins. For the Na^+ cation, such procedure gives a volumetric difference for each individual Na···Cl gap of about 2.95 $Å^3$, while for the Mg···B a much smaller value of about 0.73 $Å^3$ is obtained. Even though both compounds are clearly of ionic nature, which is evident from the

Bader charges (+1.92 and +0.82 e for Mg^{2+} and Na^{+}, –0.96 and –0.82 e for B^{-} and Cl^{-}, respectively), the difference between the two is evident. On the interatomic line between the Mg^{2+} and B^{-} ions, the boundary of the φ_k-basin is apparently located closer to the φ_{es}-boundary, resembling the strongest H1···O3 bonds in the oxalic acid dihydrate crystal, while for the Na···Cl bond is it positioned at approximately the same distance between ρ- and φ_{es}-boundaries. The corresponding values for the volumetric difference between φ_{es}- and φ_k-boundaries per each bond is equal to ca. 1.64 and 0.17 $Å^3$ for NaCl and MgB_2, respectively. This discrepancy in the size of the charge transfer gap is in a line with the different values of atomic electronegativities. In the pair of Na and Cl atoms, the difference in electronegativity is equal to 5.70 eV and 2.23 according to Mulliken and Pauling scale, respectively, while for Mg and B this difference is equal to 0.7 eV and 0.73, which is far smaller. Similarly, it is possible to estimate the number of electrons contained between the borders of different basins. For instance, within the gap between the ρ- and φ_{es}-basins in the NaCl there is ca. 0.14 e transferred from the Na to the Cl atoms. A smaller part of these electrons, ca. 0.05 e, is located between the borders of ρ- and φ_k basins. In the case of MgB_2, similar numbers were obtained, i.e., 0.12 and 0.08 electrons contained between the borders of atomic ρ- and potential φ_{es}- and φ_k-basins, respectively. The relative difference between these two numbers for the considered ionic compounds is consistent with the arrangement of atomic and potential basins borders, i.e., the closer is the φ_k-border to φ_{es}-one, the closer these two values are.

In NaCl, kinetic $\boldsymbol{F}_k(\boldsymbol{r})$ and electrostatic $\boldsymbol{F}_{es}(\boldsymbol{r})$ act on the common ρ-boundary at the position of the BCP between two atoms in opposite directions with the magnitude of about 0.33 and 0.65 a.u., respectively. The corresponding potential pseudoatoms in turn are also experiencing the pressure of these two forces, with $\boldsymbol{F}_{es}(\boldsymbol{r})$ pushing on φ_k-boundary along the interatomic line

toward the Na atom with the magnitude of ca. 0.38 a.u. near the BCP, while $\boldsymbol{F}_k(\boldsymbol{r})$ draws the electrons from inside the Cl electrostatic pseudoatom, estimated at about 0.34 a.u.

Interestingly, within the monoatomic metal layer, each Mg^{2+} cation is bonded to its closest neighbors by a total of six CP (3, –1) in $\varphi_{es}(\boldsymbol{r})$ with the corresponding φ_{es}-paths. The superposition of gradient fields of $\rho(\boldsymbol{r})$, $\varphi_{es}(\boldsymbol{r})$, and $\varphi_k(\boldsymbol{r})$ in the plane of the monoatomic Mg layer is shown in Figure S14. Although the Mg^{2+} cations are fully enclosed by the ρ-basins of B^- anions, the existence of the CP (3, –1) in $\varphi_{es}(\boldsymbol{r})$ between the metal cations suggests that they still experience the *indirect* influence of their closest metal neighbors, especially if the said neighbor is missing due to the possible structural defect frequent for metal diborides. Considering the noncovalent Cl···Cl and B···B interaction, one can note that both of them are characterized by the presence of Lagrange points, where the corresponding force is equal to zero, in the interatomic region, in particular BCPs, but not CPs (3, –1) in either $\varphi_k(\boldsymbol{r})$ or $\varphi_{es}(\boldsymbol{r})$. Instead, we observe the existence of two other types of Lagrange points located at the same place, i.e., ring CPs (3, +1) in the considered potentials between the bonded Cl atoms and ring (3, +1) and cage (3, +3) CPs in $\varphi_k(\boldsymbol{r})$ and $\varphi_{es}(\boldsymbol{r})$, respectively, between the B atoms.

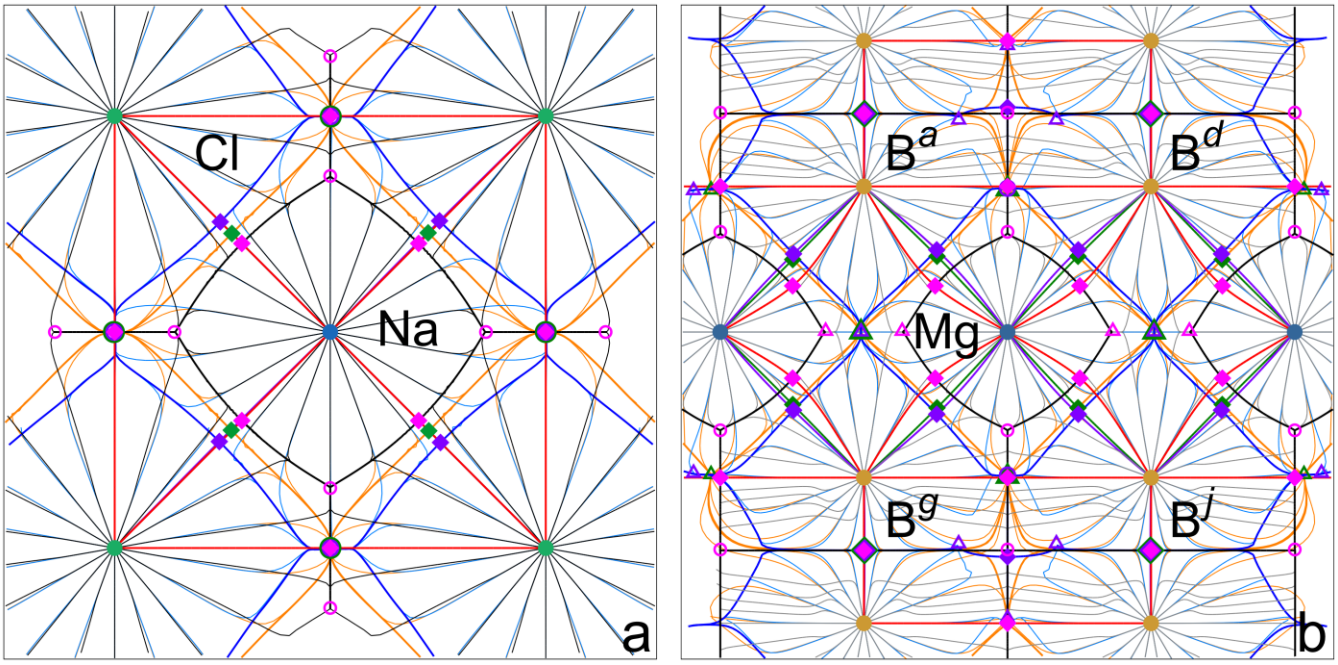

Figure 13. Superposition of gradient fields of electron density $\nabla\rho(\boldsymbol{r})$ (grey), electrostatic potential $\nabla\varphi_{es}(\boldsymbol{r})$ (blue), and kinetic potential $\nabla\varphi_{k}(\boldsymbol{r})$ (orange)calculated for the crystals of NaCl (a) and MgB_2 (b). CPs (3, –1), (3, +1), and (3, +3) are shown by rhombuses, circles, and triangles, respectively, and are colored in magenta, violet, and green for $\rho(\boldsymbol{r})$, $\varphi_{es}(\boldsymbol{r})$, and $\varphi_{k}(\boldsymbol{r})$. CPs (3, –3) coincide with the nuclear positions. Gradient paths connecting the field attractors are shown by red, violet, and green lines, respectively. For the orientation of the selected map plane for MgB_2 see Figure S11.

DISCUSSION

On the role of kinetic potential channels

One of the ways to determine atomic or ionic radii as well as a molecular boundary is to define them via the classic turning surfaces, which appear as a barrier that the classic electron within the enclosed turning surface cannot penetrate.[48] Both PAEM $\varphi_{em}(\boldsymbol{r})$[93,94] and Kohn–Sham potential[95]

can be used to determine the classical turning surfaces, either by utilizing an isovalue equal to the first ionization potential or to the energy of the highest occupied molecular orbital. Choosing the topological zero-flux criterion, one can use boundaries of φ_k-basins for bounded atoms as a surface with a similar meaning. In terms of atomic and potential basins, one could say that the corresponding static force $\mathcal{F}(\boldsymbol{r})$ keeps the electrons within the boundaries of kinetic potential basins, but not always within the atomic ρ-basins, as the space gap between the two may exist.

The kinetic potential $\varphi_k(\boldsymbol{r})$ shows well-defined channels of locally enhanced $\varphi_k(\boldsymbol{r})$ between the interacting atoms, which are accompanied by a saddle CP (3, –1) in $\varphi_k(\boldsymbol{r})$ and a corresponding φ_k-path. Hence, the heterotropic kinetic force $\boldsymbol{F}_k(\boldsymbol{r})$ pushes electrons out of atoms to these channels and thus promotes the ED localization in the internuclear space. At that, they remain within the atomic basin of an electron occupier atom (vide infra). Of course, in equilibrium, the static force $\mathcal{F}(\boldsymbol{r})$ completely compensates for the kinetic one and pushes the ED back into the atoms. These channels are distinguished by the "depth", i.e., the exact isovalue at which they would occur, and width. These two properties can be used to quantitatively describe the covalency and strength of a bond. For instance, one of the widest φ_k-channels at the given isovalue of 0.02 a.u. in Figure 14 is observed for the strongest H1···O3 hydrogen bond in the oxalic acid dihydrate crystal, which is comparable to the C–C or C–O covalent bonds. For the H2″···O2 bond, the φ_k-channel is noticeably thinner than for the H1···O3. Conversely, for the H3′···O2 H-bond no channel is observed at the chosen isovalue, despite the fact that the CP (3, –1) in $\varphi_k(\boldsymbol{r})$ as well as the corresponding φ_k-path are present. The described behaviour correlates with the estimated bond energies as we discussed above. We speculate that a φ_k-path can be treated as a route of privileged electron sharing, similar to the bond paths in $\rho(\boldsymbol{r})$, which were argued to be the channels of privileged static exchange-correlation.[13] The topological bond then, i.e., the bond path in $\rho(\boldsymbol{r})$,

does not require by default the existence of a bond path in $\varphi_k(\boldsymbol{r})$. Thus, we highlight an explicit role of kinetic factors $\varphi_k(\boldsymbol{r})$ and $\boldsymbol{F}_k(\boldsymbol{r})$ in chemical bonding, and the role of static ones $\varphi_{em}(\boldsymbol{r})$ and $\mathcal{F}(\boldsymbol{r})$ in the formation of bonded atoms.

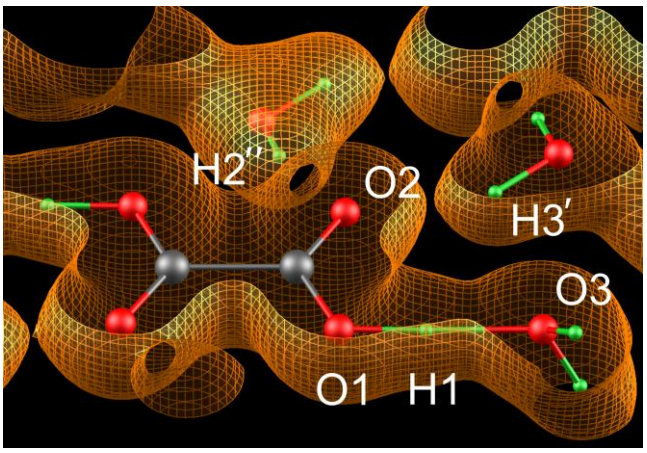

Figure 14. Isosurface of kinetic potential $\varphi_k(\boldsymbol{r})$ at 0.02 a.u. constructed around oxalic acid and the surrounding water molecules in the crystal showing the channels of locally enhanced $\varphi_k(\boldsymbol{r})$ for the presented H-bonds. Isosurfaces are cut from the top for clarity.

View on charge transfer, exchange effects, and electron sharing in terms of superposition of atomic and potential basins

Now we consider the behavior of one-electron potentials and corresponding gradient forces in conjunction with the atomic-like potential basins formed by some of them to present a more general and extensive description of the interatomic interaction in terms of mutual penetration of atomic and potential basins.

Let us to begin from a simplified case of interaction of two different atoms: e-occupier and e-contributor, which is accompanied by some degree of charge transfer. The driving force behind this process is the difference of chemical potentials μ of the two initial atoms, which in turn generates the corresponding force $\boldsymbol{F}_\mu$ acting in the direction of the lowest μ (or the highest

electronegativity χ) of the two from the e-contributor toward the e-occupier atom. One could then say that the extent of the occurring charge transfer is governed by the equilibrium state, at which the chemical potential is constant at any point $\mu_{occ}(\boldsymbol{r}) = \mu_{con}(\boldsymbol{r}) = \mu(\boldsymbol{r})$, with the latter referring to the chemical potential of the resulting system. To reach that, the total force $\boldsymbol{F}_{\mu}(\boldsymbol{r})$ approaches zero. The dominating contribution to the total force $\boldsymbol{F}_{\mu}(\boldsymbol{r})$ during the process is the homotropic force of electrostatic origin $\boldsymbol{F}_{es}(\boldsymbol{r})$, which attracts electrons formally belonging to the e-contributor to the e-occupier, and the heterotropic force of kinetic nature $\boldsymbol{F}_{k}(\boldsymbol{r})$, which pushes electrons away from the e-contributor. Consequently, both forces would promote the interatomic charge transfer. In general, the internal valence-shell structure of an e-occupier atom and the absence of such structure in e-contributor, as noted above, are direct consequences of charge transfer due to initial difference in chemical potentials. The resulting shape, volume, and general arrangement of statistically equilibrium φ_k-basins relative to ρ- and φ_{es}-basins are a direct consequence of both action of $\boldsymbol{F}_{k}(\boldsymbol{r})$ during the process of charge transfer and equilibrium condition $\boldsymbol{F}_{k}(\boldsymbol{r}) = -\mathcal{F}(\boldsymbol{r})$ That is, the electron motion effects are compensated by static force, which describes both electron-nuclear and electron-electron interactions. The expansion of a φ_k-boundary can be treated as a *response of the system against pure charge transfer* expressed as to partial or complete "sharing of transferred electrons" between the two interacting atoms. Thus, in contrast to φ_{es}-basins, the definition of φ_k-basins explicitly accounts for the exchange effects, which going further allows us to exploit this property in the real-space description of electron exchange and interatomic electron sharing commonly associated with the phenomenon of bond covalency. Additionally, applying Pauli $\varphi_P(\boldsymbol{r})$ or quantum fermionic $\varphi_f(\boldsymbol{r})$ potentials, electron pairing within the anionic φ_k-basin can be revealed.

Scheme 1 depicts a general observed arrangement of atomic and potential basins within the internuclear region of two interacting atoms: e-contributor (zone **I**) and e-occupier (zones **II**-**IV**). Four different zones of interest arranged one after the other along the interaction line can be distinguished based on the type of the enclosing boundaries and directions of action of the electronic force fields, which are marked **I** to **IV** following the route of interatomic charge transfer. The first zone **I** extends from the common zero-flux surface of $\rho(\boldsymbol{r})$ between the two atoms beyond the nucleus of the e-contributor atom, exactly occupying the whole volume of its atomic basin. Within this zone, the electrostatic $\boldsymbol{F}_{es}(\boldsymbol{r})$ and total static $\mathcal{F}(\boldsymbol{r})$ forces originated at the e-contributor draws electrons toward its nucleus, while the kinetic force $\boldsymbol{F}_{k}(\boldsymbol{r})$ pushes electrons in the opposite direction across the ρ-boundary toward the e-occupier. As we have noted previously, no complex valence-shell structure is observed in topology of the e-contributor. The zone **II**, highlighting the expansion of the φ_k-boundary, is similar to **I** in terms of directions of electrostatic and kinetic forces, except it is located within the atomic basin of the e-occupier (beyond the e-contributor atom). So, the ED within this zone actually belongs to the electron occupier. Here heterotropic kinetic force $\boldsymbol{F}_{k}(\boldsymbol{r})$, originated in the φ_k-basin of the contributor, pushes the electrons inside the occupier atom and thus acts against the homotropic electrostatic force $\boldsymbol{F}_{es}(\boldsymbol{r})$ originated in the φ_{es}-basin of an e-contributor, which in turn draws the already transferred electrons. Conversely, the neighboring zone **III**, highlighting the expansion of the φ_{es}-boundary, is conceptually different, since the electrons confined within the boundaries of φ_{es}- and φ_k-basins experience the unidirectional action of both $\boldsymbol{F}_{es}(\boldsymbol{r})$ originated at the contributor and $\boldsymbol{F}_{k}(\boldsymbol{r})$ originated at the occupier, with both acting up the φ_k-boundary towards the electron contributor. Finally, the zone **IV**, is located deeply within the atomic basin of the e-occupier atom, exactly filling the whole volume of occupier's electrostatic force field pseudoatom (occupier's φ_{es}-basin). The electrons

within this zone are under action of $\boldsymbol{F}_{es}(\boldsymbol{r})$ and $\boldsymbol{F}_{k}(\boldsymbol{r})$ forces originated at the e-occupier and directed toward or away from its nucleus, respectively. It should be noted that the common atomic zero-flux surface appears to be fully permeable by $\boldsymbol{F}_{es}(\boldsymbol{r})$, $\mathcal{F}(\boldsymbol{r})$, and $\boldsymbol{F}_{k}(\boldsymbol{r})$ originated at the electron contributor atom. Conversely, potential basin boundaries are semi-permeable: φ_k-boundary can only be penetrated by electrons drawn by $\boldsymbol{F}_{es}(\boldsymbol{r})$ of the e-contributor, while the φ_{es}-boundary only by those pushed or drawn by kinetic $\boldsymbol{F}_{k}(\boldsymbol{r})$ or static $\mathcal{F}(\boldsymbol{r})$ forces of the e-occupier.

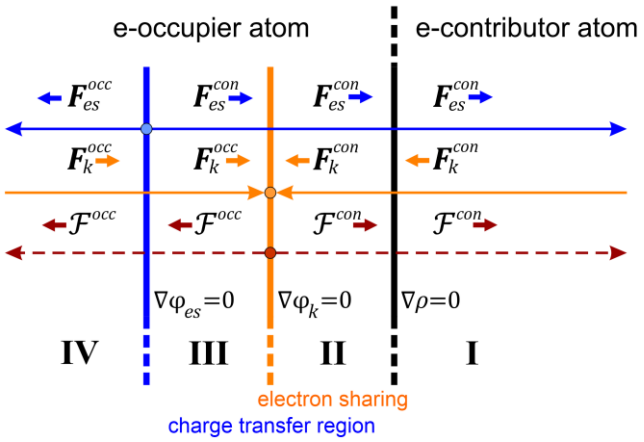

Scheme 1. A representative simplification of the relative positions of ρ- (black), φ_k- (orange), and φ_{es}- (blue) basin boundaries between the two interacting atoms: electron contributor (con) and electron occupier (occ). The directions of respective forces acting toward and away from these boundaries are indicated by the colored arrows.

As has been briefly noted above, the phenomenon of interatomic electron density transfer can be clearly identified by the presence of a gap between the boundaries of ρ- and φ_{es}-basins, a specific region of space constituted by zones **II** and **III** combined, to which the transferred electrons are confined. This is the volume enclosing an exact amount of charge captured by the e-occupier from the electroneutral bonded pseudoatom (φ_{es}-basin). The electrons captured within the charge transfer region in fact belong to the atomic basins of the e-occupier but at the same time

are experiencing the action of electrostatic force $\boldsymbol{F}_{es}(\boldsymbol{r})$ attracting them to the nucleus of the e-contributor. We found that depending on the type of interaction the relative size of zones **II** and **III** systematically changes. For all studied interatomic interactions, the following pattern was empirically confirmed: the boundary of φ_k-basin is always located at some point between the ρ- and φ_{es}-boundaries within the atomic basin of e-occupier and in extreme cases almost coincides with one or the other. This boundary thus determines what portion of the transferred electrons would be acted upon by the kinetic forces $\boldsymbol{F}_k(\boldsymbol{r})$ originated at the occupier or contributor in the same (**III**) or opposite (**II**) direction as $\boldsymbol{F}_{es}(\boldsymbol{r})$. To find the chemical meaning behind the position of φ_k-boundary, we anticipated based on the current data the existence of a direct link between the relative position of φ_k-boundary and the covalency of any bond. We proposed that a region of space enclosed by the boundaries of ρ- and φ_k-basins (**II**), being part of the transfer region, can be considered as an area of sharing of the transferred electrons between two interacting atoms. In other words, contributor's φ_k-basin always penetrates occupier's ρ-basin approaching occupier's φ_{es}-basin, which manifests electron exchange effects imposed on the transferred electrons. Thus, the φ_{es}-boundary distinguishes regions where exchange effects can be attributed to a particular atom: a contributor serves zones **I** and **II**, while an occupier serves **III** and **IV**. Further, thus defined region of electron sharing of the transferred electrons (**II**) appeared to be separated from the φ_{es}-basin of an electron occupier (**IV**) by the inner part of the charge transfer region (**III**). This consideration was prompted by the empirical fact that φ_k-boundaries practically approach φ_{es}-ones for covalent bonds excluding an area (**III**) where occupier's kinetic force $\boldsymbol{F}_k(\boldsymbol{r})$ pushes transferred electrons out its φ_{es}-basin. For the stronger noncovalent interactions, such as a classical H-bond or coordination bonds, for which the high covalency is expected, area **III** is far smaller than **II**. For the weaker H-bonds, the corresponding region of sharing (**II**) is smaller and the bond

itself is less covalent. Interestingly, for the O–H covalent bond involved in strong hydrogen bonding, the appearance of zone **III** reducing the extent of electron sharing could be noted to some extent.

Additional clarifications need to be made regarding the nonpolar covalent and ionic bonds. As we have reiterated multiple times throughout the text, the space gap between the boundaries of ρ- and φ_k-basins can only be equated to the sharing of transferred ED but not to the traditionally accepted concept of electron sharing between bonded atoms. With this, the proposed scheme is by definition not applicable to nonpolar covalent bonds, such as C–C or B–B ones. Considering the ionic Na···Cl and Mg···B bonds, we note that the ED found within the wide region of space enclosed by ρ- and φ_k-boundaries, if considered shared between bonded atoms, may raise questions or doubts. Specifically, although the mutual arrangement of atomic and potential basin boundaries in MgB_2 is similar to a one found for strong hydrogen bonds, the Mg···B interaction is of predominantly ionic nature, which for example is supported by the analysis of delocalization indices performed for various metal diborides by Wagner et al.[96] Rather, the observed picture probably needs to be treated as a manifestation of electron pairing occurring as a result of charge transfer, which is supported by the analysis of Pauli and exchange potentials, showing their respective minima and linear segments along the bond paths. On the other hand, our data indicate the obvious operation of the donor-acceptor mechanism of interaction between ions in the studied compounds, which should manifest itself in the sharing of the transferred ED. Similarly to H-bonds, the occupier atoms (O, Cl, and B) play the role of a donor, while the contributors (H, Na, and Mg) act as an acceptor. Nevertheless, both ways of description do not actually contradict each other but only represent different views on the manifestation of exchange effects for ionic and donor-acceptor bonds.

Notably, the Ehrenfest force $\mathfrak{F}(\boldsymbol{r})$ is the average of the instantaneous force over the positions of the rest electrons and is not related to gradient field, while the forces $\mathcal{F}(\boldsymbol{r})$ and $\boldsymbol{F}_k(\boldsymbol{r})$ are originated from the PAEM φ_{em} and the kinetic potential φ_k, respectively. Let us recall that $\mathcal{F}(\boldsymbol{r})$ and $\boldsymbol{F}_k(\boldsymbol{r})$ are attributed to atoms and their mutual balance in an equilibrium system is outlined by the boundary of kinetic basins: The static force $\mathcal{F}(\boldsymbol{r})$, like the Ehrenfest force, is directed toward the nucleus seeking to neutralize the electric charge and keeps electrons in atomic basins, while the kinetic force $\boldsymbol{F}_k(\boldsymbol{r})$ pushes electrons away from the nucleus. As noted by Martín Pendás with co-workers,[52,53] the PAEM-derived gradient force field $\mathcal{F}(\boldsymbol{r})$ is very similar to the vector field of one-electron Ehrenfest force $\mathfrak{F}(\boldsymbol{r})$. They discussed the topology of Ehrenfest force field $\mathfrak{F}(\boldsymbol{r})$ and compared it with the gradient field of ED $\nabla\rho(\boldsymbol{r})$. As a result, they concluded that although $\mathfrak{F}(\boldsymbol{r})$ and $\nabla\rho(\boldsymbol{r})$ are usually homeomorphic, this is not always the case. Further, when the two fields are superimposed onto each other, the gaps between boundaries of the atomic-like $\mathfrak{F}$-basins and atomic ρ-basins are clearly visible for polar bonds, which resemble the gaps found between the boundaries of e-occupier's φ_k- and ρ-basins. Similarly, the kinetic $\boldsymbol{F}_k(\boldsymbol{r})$ and static $\mathcal{F}(\boldsymbol{r})$ force fields (omitting the force direction) turn out to not always be homeomorphic with ED gradient field $\nabla\rho(\boldsymbol{r})$. Both kinetic and Ehrenfest force fields pseudoatoms bear smaller nominal charges than matching Bader's quantum atoms. Moreover, the volume of φ_k- and $\mathfrak{F}$-basins generally shows the same trend comparing to corresponding ρ-basins being larger or smaller for electropositive or electronegative atoms, respectively. Hence, the force fields $\mathcal{F}(\boldsymbol{r})$ and $\boldsymbol{F}_k(\boldsymbol{r})$ contain similar quantum chemical information as $\mathfrak{F}(\boldsymbol{r})$ and could be used as a substitute for latter within orbital-free density functional theory and experimental quantum crystallography to estimate the force acting on an electron in a molecule or crystal owing to the presence of the nuclei and remaining electrons.

In summary, the proposed approach to real-space partitioning of many-nuclear many-electron systems into the union of atomic and atomic-like potential basins allows one to reveal a conceptually novel and physically grounded description of interatomic interaction accompanied by charge transfer and electron exchange. In particular, it allows one to obtain an unambiguous definition of the charge transfer and electron sharing by highlighting the region in space where the respective phenomena occur. The observed experimental picture can be fully described by the proposed scheme, with no exceptions so far, including the already published results obtained either through experimental X-ray diffraction data, where the superposition of gradient fields of $\nabla\rho(\boldsymbol{r})$, $\nabla\varphi_{es}(\boldsymbol{r})$, and $\nabla\varphi_{k}(\boldsymbol{r})$ was constructed for the uracil derivative crystal,[15] or mentioned gas-phase theoretical calculations of $\varphi_{es}(\boldsymbol{r})$ and $\varphi_{em}(\boldsymbol{r})$ potentials along covalent and noncovalent bonds involving halogen, chalcogen, and pnictogen atoms.[84,97] From our point of view, the presented scheme extends the functionality of QTAIMC by providing the space gaps between the boundaries of atomic and potential basins, which are by default missing from the theory. In this way, it becomes clearer to understand how the non-overlapping QTAIMC basins hold together forming molecules and crystals.

COMPUTATIONAL METHODS

Experimental static ED distributions were restored via multipole models for crystalline oxalic acid dihydrate $(COOH)_2 \times 2H_2O$, sodium chloride (NaCl),[22] magnesium diboride (MgB_2),[81] and 1-{2-[2-(methoxycarbonylmethylsulfonyl)ethoxy]ethyl}-3,5-dimethylisocyanurate (*ica*).[15] For crystals of oxalic acid dihydrate, the remeasured data, which are in full accordance with the latest published results[87] have been used. It should be noted that magnesium diboride is a nonstoichiometric compound with the exact composition of $Mg_{0.955}B_2$, so the modeled experimental ED is averaged

over the crystal. The multipole model parameters for the last three compounds were adopted from our previous works. Henceforth, we will analyze the bonding features of these structures and compare them. A partial numbering scheme is presented in SI.

Analysis of the scalar fields

Analysis of multipole-modeled ED was performed using the *WinXPRO* v3.4.46, *3DPlot* v2.5.25, and *TrajPlot* v.1.4.0.2 software.[86,98,99] Calculations were performed according to the published procedures.[15] For all compounds, an appropriate electroneutral spherical cluster was constructed with a radius of more than 10 Å.

The search for CPs in scalar fields of $\rho(\boldsymbol{r})$, $\varphi_{es}(\boldsymbol{r})$, $\varphi_{em}(\boldsymbol{r})$, and $\varphi_k(\boldsymbol{r})$ was performed along the interatomic lines between symmetrically independent atoms with the maximal "atom-atom" distance of 4.5 Å. Interaction energies (in kcal mol^{-1}) for hydrogen bonds and weak noncovalent interactions were estimated via the correlation $E_g = 269.2014 \cdot g(\boldsymbol{r}_b)$ with the kinetic energy density $g(\boldsymbol{r})$ (in a.u.) at a BCP,[100] which in turn was approximated according to Kirzhnits.[101] Atomic ρ-basins and atomic-like potential φ_{es}- and φ_k-basins were defined with tolerance on an interatomic surface radius of $5 \cdot 10^{-5}$ Å. Angular parameters $n\theta$ and $n\varphi$ defining the number of grid points inside a β-sphere were set to 96 and 120, respectively. An increment factor for the BCP search was equal to 0.1 Å. Gradient vector trajectories of $\rho(\boldsymbol{r})$, $\varphi_{es}(\boldsymbol{r})$, and $\varphi_k(\boldsymbol{r})$ were calculated with the following parameters: a step along the gradient path equal to 0.01 Å, an out-of-plane distance up to 0.5 Å, and a cut-off value for gradient path termination $|\nabla f(\boldsymbol{r})|$ of $0.1 \cdot 10^{-5}$ e Å^{-4} and e Å^{-2}, respectively.

One-dimensional profiles of various functions along bond paths were calculated using the grid step length of 0.01 Å or less. Two- and three-dimensional distributions were calculated within

the constructed atomic clusters with a step size of 0.05 Å or smaller. If not stated otherwise, all functions utilized within this work were computed according to the formulae presented in the Introduction. Von Weizsäcker potential $\varphi_W(\boldsymbol{r})$ was calculated using the exact expression.[39,40] Electrostatic potential $\varphi_{es}(\boldsymbol{r})$ was computed within the finite electroneutral cluster.[102,103] It should be noted that the obtained values of $\varphi_{es}(\boldsymbol{r})$ and related functions (see above), such as $\varphi_{em}(\boldsymbol{r})$, $\varphi_k(\boldsymbol{r})$, and $\varphi_P(\boldsymbol{r})$, are affected by the size of an atomic cluster, location of point $\boldsymbol{r}$ relative to the cluster center, and charge asymmetry. Therefore, for each individual compound, the largest possible spherical cluster was constructed to simulate the symmetrical electroneutral crystalline environment. The difference between properties $\varphi_{es}(\boldsymbol{r})$, $\varphi_{em}(\boldsymbol{r})$, $\varphi_k(\boldsymbol{r})$, and $\varphi_P(\boldsymbol{r})$ calculated along the bond paths for the symmetry-related pairs of intermolecular contacts of the central molecule was less than 0.01 a.u. The Pauli potential $\varphi_P(\boldsymbol{r})$ was computed according to the published procedure[46] taking empirical chemical potential $\mu = \sum_k \mu_k N_k \,/\, \sum_k N_k$, where N_k is the number of electron of the atom k in the unit cell.[23] The same approximation was utilized for the calculation of kinetic potential $\varphi_k(\boldsymbol{r})$. Individual atomic chemical potentials were taken as a negative of first ionization potentials.[104] This approximation underestimates μ by approximately 10 %. If not stated otherwise, for the calculation of local exchange potential $\varphi_x(\boldsymbol{r})$ orbital-free local density approximation of von Barth–Hedin[105] was used. For the sake of comparison, one-dimensional profiles of various potentials along the lines of covalent and hydrogen bonds calculated using the approximations of von Barth–Hedin,[105] van Leeuwen and Baerends[106], and Becke[107], as well as directly from the wavefunctions (ωB97X-D/aug-cc-pVTZ) are presented in Figures S15 and S16. For the analysis of theoretical data, *TOPOND*[108] and *Multiwfn* 3.8[109] were used.

CONCLUSIONS

From the point of view of a chemist, the quantum theory of atoms in molecules and crystals provides probably the most intuitive, familiar, and understandable scheme of partitioning molecular or crystalline position space into bonded atoms. Among the other things, the ability to explicitly visualize the topological portrait of electron density using the bond path network, similar to how one would draw a bond line, brought it its well-deserved popularity. By extending the powerful ideas of quantum chemical topology to other scalar fields besides the electron density, such as electrostatic $\varphi_{es}(\boldsymbol{r})$ and one-electron kinetic $\varphi_k(\boldsymbol{r})$ potentials, one can retrieve conceptually new information about chemical interactions, for instance by comparing the shapes, volumes, and charges of the pseudoatoms defined in the electrostatic and kinetic force fields (potential-based basins), analogs of quantum topological atoms.

The presence or the absence of Lagrange saddle critical points in the potentials and potential paths arising from these points and connecting pairs of atoms can help one better understand the underlying mechanisms of chemical interactions. For example, a saddle CP (3, –1) in $\varphi_k(\boldsymbol{r})$ and a corresponding φ_k-path testify the existence of a well-defined channel of locally enhanced kinetic potential formed between the interacting atoms, which is assumed to be a path of privileged electron sharing between atoms. Inside such a channel the heterotropic kinetic force $\boldsymbol{F}_k(\boldsymbol{r})$ pushes electrons away from the atomic nuclei and thus promotes the electron localization in the internuclear space, while the homotropic static force $\mathcal{F}(\boldsymbol{r})$ in the statistically equilibrium systems completely compensates for the kinetic one and pushes the electron density back to the atomic nuclei.

In this work, we considered the superpositions of atomic and potential atomic-like basins in different kinds of chemical compounds. We found several general patterns, which are applicable to any kind of chemical interactions. For polar interactions, two types of participating atoms, i.e.,

electron occupier and electron contributor, can be distinguished. The former is always characterized by a complex internal structure, that is the boundaries of potential basins are located within its atomic basin. Additionally, the φ_k-basin boundary is always positioned between the other two, approaching either ρ- or φ_{es}-boundary depending on the type of interaction. For any polar covalent bond, the boundary of electrostatic and kinetic-force pseudoatoms almost coincide, but the ρ-boundary stands individually. For a polar noncovalent interaction, φ_k-boundary is shifted away from the φ_{es}-boundary, separating the charge transfer region into two smaller ones. Continuing with the elegant simplicity of QTAIMC, we assigned chemical meaning to these gaps between the boundaries of atomic and potential basins. The region of space between the two interacting atoms enclosed by the boundaries of φ_{es}- and ρ-basins is identified as a region of charge transfer due to the known property of $\varphi_{es}(\boldsymbol{r})$ of defining zero-charged bonded pseudoatoms. We proposed that the gap between the boundaries of the ρ- and φ_k-pseudoatoms represents a region of sharing of transferred electrons since the definition of φ_k-basins explicitly accounts for the exchange effects, which are absent in φ_{es}-basins. This conjecture is supported by both empirical evidences, i.e., the observed boundary arrangement of atomic and potential-based basins for various types of interaction, as well as the distribution of electronic potentials, in particular, von Weizsäcker, Pauli, and exchange-correlation ones. We suggest that the specific arrangement of topological pseudoatomic boundaries is a response of a system to an occurred charge transfer, while the exact position of φ_k-basin boundary describes the kinetic contribution electron exchange as a volumetric characteristic, i.e., a fraction of transferred electrons shared between the two interacting atoms.

Thus, our approach to real-space partitioning of many-nuclear many-electron systems into the union of atomic and atomic-like potential basins allows one to reveal a conceptually novel and

physically grounded description of interatomic interaction accompanied by charge transfer. Importantly, the superposition of atomic and potential basins of different nature explains how non-overlapping bounded space-filling quantum atoms hold together via the gaps between bounded atoms and force fields pseudoatoms.

ASSOCIATED CONTENT

The following file is available free of charge.

One-dimensional profiles, contour maps, and three-dimensional distributions of various functions; representations of atomic and potential basins and molecular graphs; tabulated data on volumes of atomic and potential basins and charges integrated over them (PDF)

AUTHOR INFORMATION

Corresponding Author

*Email: robert.fayzullin@gmail.com (R. R. F.).

ORCID

Sergey A. Shteingolts: 0000-0001-6265-5684

Adam I. Stash: 0000-0001-7901-5851

Vladimir G. Tsirelson: 0000-0002-8610-9116

Robert R. Fayzullin: 0000-0002-3740-9833

Author Contributions

The manuscript was written through contributions of all authors. All authors have given approval to the final version of the manuscript.

Funding Source

Russian Science Foundation, grant No. 21-73-10191

Ministry of Science and Higher Education of the Russian Federation, project FENU2020-0019.

Notes

The authors declare no competing financial interest.

ACKNOWLEDGMENT

S. A. S. and R. R. F. acknowledge the support of the Russian Science Foundation (grant No. 21-73-10191, https://rscf.ru/en/project/21-73-10191/). A. I. S. worked within the government statements for the Nesmeyanov Institute and is grateful to the Ministry of Science and Higher Education of the Russian Federation. V. G. T. worked within the project FENU2020-0019 of the Ministry of Science and Higher Education of the Russian Federation.

ABBREVIATIONS

BCP, bond critical point; CP, critical point; e-contributor, electron contributor; ED, electron density; e-occupier, electron occupier; FAEM, force acting on an electron in a molecule; *ica*, 1-{2-[2-(methoxycarbonylmethylsulfonyl)ethoxy]ethyl}-3,5-dimethylisocyanurate; PAEM, potential acting on an electron in a molecule; QTAIMC, quantum theory of atoms in molecules and crystals; VSCC, valence shell charge concentrations.

REFERENCES

(1) Bader, R. F. W.; Nguyen-Dang, T. T. Quantum Theory of Atoms in Molecules–Dalton Revisited. In *Advances in Quantum Chemistry*; 1981; Vol. 14, pp 63–124. https://doi.org/10.1016/S0065-3276(08)60326-3.

(2) Bader, R. F. W.; Carroll, M. T.; Cheeseman, J. R.; Chang, C. Properties of Atoms in Molecules: Atomic Volumes. *J. Am. Chem. Soc.* **1987**, *109* (26), 7968–7979. https://doi.org/10.1021/ja00260a006.

(3) Bader, R. F. W. Atoms in Molecules. *Acc. Chem. Res.* **1985**, *18* (1), 9–15. https://doi.org/10.1021/ar00109a003.

(4) Bader, R. F. W. W. A Quantum Theory of Molecular Structure and Its Applications. *Chem. Rev.* **1991**, *91* (5), 893–928. https://doi.org/10.1021/cr00005a013.

(5) Bader, R. F. W. *Atoms in Molecules: A Quantum Theory*; Clarendon Press: Oxford, 1990.

(6) Bader, R. F. W.; Popelier, P. L. A.; Keith, T. A. Theoretical Definition of a Functional Group and the Molecular Orbital Paradigm. *Angew. Chem. Int. Ed.* **1994**, *33* (6), 620–631. https://doi.org/10.1002/anie.199406201.

(7) Bader, R. F. W. The Quantum Mechanical Basis of Conceptual Chemistry. *Monatsh. Chem.* **2005**, *136* (6), 819–854. https://doi.org/10.1007/s00706-005-0307-x.

(8) Matta, C. F.; Bader, R. F. W. An Experimentalist's Reply to "What Is an Atom in a Molecule?" *J. Phys. Chem. A* **2006**, *110* (19), 6365–6371. https://doi.org/10.1021/jp060761+.

(9) Bader, R. F. W.; Matta, C. F. Atoms in Molecules as Non-Overlapping, Bounded, Space-

Filling Open Quantum Systems. *Found. Chem.* **2013**, *15* (3), 253–276. https://doi.org/10.1007/s10698-012-9153-1.

(10) Bader, R. F. W. A Bond Path: A Universal Indicator of Bonded Interactions. *J. Phys. Chem. A* **1998**, *102* (37), 7314–7323. https://doi.org/10.1021/jp981794v.

(11) Keith, T. A.; Bader, R. F. W.; Aray, Y. Structural Homeomorphism between the Electron Density and the Virial Field. *Int. J. Quantum Chem.* **1996**, *57* (2), 183–198. https://doi.org/10.1002/(SICI)1097-461X(1996)57:2<183::AID-QUA4>3.0.CO;2-U.

(12) Tsirelson, V. G. Interpretation of Experimental Electron Densities by Combination of the QTAMC and DFT. In *The Quantum Theory of Atoms in Molecules*; Wiley-VCH Verlag GmbH & Co. KGaA: Weinheim, Germany, 2007; pp 257–283. https://doi.org/10.1002/9783527610709.ch10.

(13) Martín Pendás, A.; Francisco, E.; Blanco, M. A.; Gatti, C. Bond Paths as Privileged Exchange Channels. *Chem. Eur. J.* **2007**, *13* (33), 9362–9371. https://doi.org/10.1002/chem.200700408.

(14) Tsirelson, V. G.; Shishkina, A. V.; Stash, A. I.; Parsons, S. The Experimental and Theoretical QTAIMC Study of the Atomic and Molecular Interactions in Dinitrogen Tetroxide. *Acta Crystallogr. Sect. B Struct. Sci.* **2009**, *65* (5), 647–658. https://doi.org/10.1107/S0108768109028821.

(15) Shteingolts, S. A.; Stash, A. I.; Tsirelson, V. G.; Fayzullin, R. R. Orbital-Free Quantum Crystallographic View on Noncovalent Bonding: Insights into Hydrogen Bonds, Π···π and Reverse Electron Lone Pair···π Interactions. *Chem. Eur. J.* **2021**, *27* (28), 7789–7809.

https://doi.org/10.1002/chem.202005497.

(16) Tsirelson, V.; Stash, A. On Functions and Quantities Derived from the Experimental Electron Density. *Acta Crystallogr., Sect. A: Found. Crystallogr.* **2004**, *60* (5), 418–426. https://doi.org/10.1107/S010876730401339X.

(17) Shteingolts, S. A.; Voronina, J. K.; Saifina, L. F.; Shulaeva, M. M.; Semenov, V. E.; Fayzullin, R. R. On the Transfer of Theoretical Multipole Parameters for Restoring Static Electron Density and Revealing and Treating Atomic Anharmonic Motion. Features of Chemical Bonding in Crystals of an Isocyanuric Acid Derivative. *Acta Crystallogr., Sect. B: Struct. Sci. Cryst. Eng. Mater.* **2021**, *77* (6), 871–891. https://doi.org/10.1107/S2052520621009690.

(18) Bader, R. F. W.; Matta, C. F. Bonding to Titanium. *Inorg. Chem.* **2001**, *40* (22), 5603–5611. https://doi.org/10.1021/ic010165o.

(19) Popelier, P. L. A. A. Quantum Chemical Topology: On Bonds and Potentials. In *Structure and Bonding*; 2005; Vol. 115, pp 1–56. https://doi.org/10.1007/b135617.

(20) Farrugia, L. J.; Evans, C.; Tegel, M. Chemical Bonds without "Chemical Bonding"? A Combined Experimental and Theoretical Charge Density Study on an Iron Trimethylenemethane Complex. *J. Phys. Chem. A* **2006**, *110* (25), 7952–7961. https://doi.org/10.1021/jp061846d.

(21) Tognetti, V.; Joubert, L. On the Physical Role of Exchange in the Formation of an Intramolecular Bond Path between Two Electronegative Atoms. *J. Chem. Phys.* **2013**, *138* (2), 024102. https://doi.org/10.1063/1.4770495.

(22) Tsirelson, V.; Stash, A. Orbital-Free Quantum Crystallography: View on Forces in Crystals. *Acta Crystallogr. Sect. B Struct. Sci. Cryst. Eng. Mater.* **2020**, *76* (5), 769–778. https://doi.org/10.1107/S2052520620009178.

(23) Tsirelson, V.; Stash, A. Developing Orbital-Free Quantum Crystallography: The Local Potentials and Associated Partial Charge Densities. *Acta Crystallogr., Sect. B: Struct. Sci. Cryst. Eng. Mater.* **2021**, *77* (4), 467–477. https://doi.org/10.1107/s2052520621005540.

(24) Massa, L.; Huang, L.; Karle, J. Quantum Crystallography and the Use of Kernel Projector Matrices. *Int. J. Quantum Chem.* **1995**, *56* (S29), 371–384. https://doi.org/10.1002/qua.560560841.

(25) Tsirelson, V. G. Topological Analysis of the Experimental Electron Density. *Can. J. Chem.* **1996**, *74* (6), 1171–1179. https://doi.org/10.1139/v96-131.

(26) Gatti, C. Chemical Bonding in Crystals: New Directions. *Z. Kristallogr.* **2005**, *220* (5–6), 399–457. https://doi.org/10.1524/zkri.220.5.399.65073.

(27) Macchi, P. Modern Charge Density Studies: The Entanglement of Experiment and Theory. *Crystallogr. Rev.* **2013**, *19* (2), 58–101. https://doi.org/10.1080/0889311X.2013.785538.

(28) Grabowsky, S.; Genoni, A.; Bürgi, H. B. Quantum Crystallography. *Chem. Sci.* **2017**, *8* (6), 4159–4176. https://doi.org/10.1039/c6sc05504d.

(29) Genoni, A.; Bučinský, L.; Claiser, N.; Contreras-García, J.; Dittrich, B.; Dominiak, P. M.; Espinosa, E.; Gatti, C.; Giannozzi, P.; Gillet, J. M.; Jayatilaka, D.; Macchi, P.; Madsen, A.; Massa, L.; Matta, C. F.; Merz, K. M.; Nakashima, P. N. H.; Ott, H.; Ryde, U.; Schwarz, K.;

Sierka, M.; Grabowsky, S. Quantum Crystallography: Current Developments and Future Perspectives. *Chem. Eur. J.* **2018**, *24* (43), 10881–10905. https://doi.org/10.1002/chem.201705952.

(30) Macchi, P. The Connubium between Crystallography and Quantum Mechanics. *Crystallogr. Rev.* **2020**, *26* (4), 209–268. https://doi.org/10.1080/0889311X.2020.1853712.

(31) Genoni, A.; Macchi, P. Quantum Crystallography in the Last Decade: Developments and Outlooks. *Crystals* **2020**, *10* (6), 1–20. https://doi.org/10.3390/cryst10060473.

(32) Slamet, M.; Sahni, V.; Harbola, M. K. Force Field and Potential Due to the Fermi-Coulomb Hole Charge for Nonspherical-Density Atoms. *Phys. Rev. A* **1994**, *49* (2), 809–817. https://doi.org/10.1103/PhysRevA.49.809.

(33) Liu, S.; Ayers, P. W.; Parr, R. G. Alternative Definition of Exchange-Correlation Charge in Density Functional Theory. *J. Chem. Phys.* **1999**, *111* (14), 6197–6203. https://doi.org/10.1063/1.479924.

(34) Sen, K. D.; De Proft, F.; Geerlings, P. Applications of Electrostatic Interpretation of Components of Effective Kohn–Sham Potential in Atoms. *J. Chem. Phys.* **2002**, *117* (10), 4684–4693. https://doi.org/10.1063/1.1497679.

(35) March, N. H. The Local Potential Determining the Square Root of the Ground-State Electron Density of Atoms and Molecules from the Schrödinger Equation. *Phys. Lett. A* **1986**, *113* (9), 476–478. https://doi.org/10.1016/0375-9601(86)90123-4.

(36) March, N. H. The Density Amplitude P½ and the Potential Which Generates It. *J. Comput.*

Chem. **1987**, *8* (4), 375–379. https://doi.org/10.1002/jcc.540080414.

(37) March, N. H. Concept of the Pauli Potential in Density Functional Theory. *J. Mol. Struct. THEOCHEM* **2010**, *943* (1–3), 77–82. https://doi.org/10.1016/j.theochem.2009.10.030.

(38) King, R. A.; Handy, N. C. Kinetic Energy Functionals from the Kohn–Sham Potential. *Phys. Chem. Chem. Phys.* **2000**, *2* (22), 5049–5056. https://doi.org/10.1039/b005896n.

(39) Hunter, G. The Exact One-Electron Model of Molecular Structure. *Int. J. Quantum Chem.* **1986**, *29* (2), 197–204. https://doi.org/10.1002/qua.560290209.

(40) Herring, C. Explicit Estimation of Ground-State Kinetic Energies from Electron Densities. *Phys. Rev. A* **1986**, *34* (4), 2614–2631. https://doi.org/10.1103/PhysRevA.34.2614.

(41) Liu, S. Steric Effect: A Quantitative Description from Density Functional Theory. *J. Chem. Phys.* **2007**, *126* (24), 244103. https://doi.org/10.1063/1.2747247.

(42) Tsirelson, V. G.; Stash, A. I.; Liu, S. Quantifying Steric Effect with Experimental Electron Density. *J. Chem. Phys.* **2010**, *133* (11), 114110. https://doi.org/10.1063/1.3492377.

(43) Hunter, G. Conditional Probability Amplitudes in Wave Mechanics. *Int. J. Quantum Chem.* **1975**, *9* (2), 237–242. https://doi.org/10.1002/qua.560090205.

(44) Gritsenko, O.; van Leeuwen, R.; Baerends, E. J. Analysis of Electron Interaction and Atomic Shell Structure in Terms of Local Potentials. *J. Chem. Phys.* **1994**, *101* (10), 8955–8963. https://doi.org/10.1063/1.468024.

(45) Nagy, Á. The Pauli Potential from the Differential Virial Theorem. *Int. J. Quantum Chem.* **2010**, *110* (12), 2117–2120. https://doi.org/10.1002/qua.22497.

(46) Tsirelson, V. G.; Stash, A. I.; Karasiev, V. V.; Liu, S. Pauli Potential and Pauli Charge from Experimental Electron Density. *Comput. Theor. Chem.* **2013**, *1006*, 92–99. https://doi.org/10.1016/j.comptc.2012.11.015.

(47) Ludeña, E. V.; Arroyo, D.; Salazar, E. X.; Vallejo, J. The Kinetic Energy Pauli Enhancement Factor and Its Role in Determining the Shell Structure of Atoms and Molecules. In *Advances in Quantum Chemistry*; 2018; Vol. 76, pp 59–78. https://doi.org/10.1016/bs.aiq.2017.05.002.

(48) Yang, Z.-Z.; Davidson, E. R. Evaluation of a Characteristic Atomic Radius by an Ab Initio Method. *Int. J. Quantum Chem.* **1997**, *62* (1), 47–53. https://doi.org/10.1002/(SICI)1097-461X(1997)62:1<47::AID-QUA5>3.0.CO;2-3.

(49) Yang, Z. Z.; Zhao, D. X. A Characteristic Molecular Contour Evaluated by a Theoretical Method. *Chem. Phys. Lett.* **1998**, *292* (4–6), 387–393. https://doi.org/10.1016/S0009-2614(98)00747-7.

(50) Zhang, M.-B.; Zhao, D.-X.; Yang, Z.-Z. The Characteristic Boundary Radii of Atoms. *J. Theor. Comput. Chem.* **2005**, *04* (01), 281–288. https://doi.org/10.1142/S0219633605001568.

(51) Zhao, D. X.; Yang, Z. Z. Theoretical Exploration of the Potential and Force Acting on One Electron within a Molecule. *J. Phys. Chem. A* **2014**, *118* (39), 9045–9057. https://doi.org/10.1021/jp5020466.

(52) Martín Pendás, A.; Hernández-Trujillo, J. The Ehrenfest Force Field: Topology and Consequences for the Definition of an Atom in a Molecule. *J. Chem. Phys.* **2012**, *137* (13),

134101. https://doi.org/10.1063/1.4755326.

(53) Martín Pendás, A.; Francisco, E.; Gallo Bueno, A.; Guevara Vela, J. M.; Costales, A. Emergent Scalar and Vector Fields in Quantum Chemical Topology. In *Applications of Topological Methods in Molecular Chemistry*; Chauvin, R., Lepetit, C., Silvi, B., Alikhani, E., Eds.; Springer International Publishing: Cham, 2016; pp 131–150. https://doi.org/10.1007/978-3-319-29022-5_6.

(54) Tsirelson, V. G.; Avilov, A. S.; Lepeshov, G. G.; Kulygin, A. K.; Stahn, J.; Pietsch, U.; Spence, J. C. H. Quantitative Analysis of the Electrostatic Potential in Rock-Salt Crystals Using Accurate Electron Diffraction Data. *J. Phys. Chem. B* **2001**, *105* (21), 5068–5074. https://doi.org/10.1021/jp0015729.

(55) Szarek, P.; Tachibana, A. The Field Theoretical Study of Chemical Interaction in Terms of the Rigged QED: New Reactivity Indices. *J. Mol. Model.* **2007**, *13* (6–7), 651–663. https://doi.org/10.1007/s00894-007-0215-6.

(56) Tsirelson, V.; Ivanov, Y.; Zhurova, E.; Zhurov, V.; Tanaka, K. Electron Density of KNiF3: Analysis of the Atomic Interactions. *Acta Crystallogr. Sect. B Struct. Sci.* **2000**, *56* (2), 197–203. https://doi.org/10.1107/S0108768199015529.

(57) Zhurova, E. A.; Zuo, J. M.; Tsirelson, V. G. Topological Analysis of Electrostatic Potential in SrTiO3. *J. Phys. Chem. Solids* **2001**, *62* (12), 2143–2146. https://doi.org/10.1016/S0022-3697(01)00171-8.

(58) Mata, I.; Molins, E.; Espinosa, E. Zero-Flux Surfaces of the Electrostatic Potential: The Border of Influence Zones of Nucleophilic and Electrophilic Sites in Crystalline

Environment. *J. Phys. Chem. A* **2007**, *111* (39), 9859–9870. https://doi.org/10.1021/jp074032l.

(59) Mata, I.; Molins, E.; Alkorta, I.; Espinosa, E. Topological Properties of the Electrostatic Potential in Weak and Moderate N···H Hydrogen Bonds. *J. Phys. Chem. A* **2007**, *111* (28), 6425–6433. https://doi.org/10.1021/jp071924c.

(60) Mata, I.; Alkorta, I.; Molins, E.; Espinosa, E. Electrostatics at the Origin of the Stability of Phosphate-Phosphate Complexes Locked by Hydrogen Bonds. *ChemPhysChem* **2012**, *13* (6), 1421–1424. https://doi.org/10.1002/cphc.201200068.

(61) Shishkina, A. V.; Zhurov, V. V.; Stash, A. I.; Vener, M. V.; Pinkerton, A. A.; Tsirelson, V. G. Noncovalent Interactions in Crystalline Picolinic Acid N-Oxide: Insights from Experimental and Theoretical Charge Density Analysis. *Cryst. Growth Des.* **2013**, *13* (2), 816–828. https://doi.org/10.1021/cg3015223.

(62) Bertolotti, F.; Shishkina, A. V.; Forni, A.; Gervasio, G.; Stash, A. I.; Tsirelson, V. G. Intermolecular Bonding Features in Solid Iodine. *Cryst. Growth Des.* **2014**, *14* (7), 3587–3595. https://doi.org/10.1021/cg5005159.

(63) Bartashevich, E. V.; Yushina, I. D.; Stash, A. I.; Tsirelson, V. G. Halogen Bonding and Other Iodine Interactions in Crystals of Dihydrothiazolo(Oxazino)Quinolinium Oligoiodides from the Electron-Density Viewpoint. *Cryst. Growth Des.* **2014**, *14* (11), 5674–5684. https://doi.org/10.1021/cg500958q.

(64) Mata, I.; Molins, E.; Alkorta, I.; Espinosa, E. The Paradox of Hydrogen-Bonded Anion–Anion Aggregates in Oxoanions: A Fundamental Electrostatic Problem Explained in Terms

of Electrophilic···Nucleophilic Interactions. *J. Phys. Chem. A* **2015**, *119* (1), 183–194. https://doi.org/10.1021/jp510198g.

(65) Alkorta, I.; Mata, I.; Molins, E.; Espinosa, E. Charged versus Neutral Hydrogen-Bonded Complexes: Is There a Difference in the Nature of the Hydrogen Bonds? *Chem. Eur. J.* **2016**, *22* (27), 9226–9234. https://doi.org/10.1002/chem.201600788.

(66) Bartashevich, E.; Stash, A.; Yushina, I.; Minyaev, M.; Bol'shakov, O.; Rakitin, O.; Tsirelson, V. Bonding Features in Appel's Salt from the Orbital-Free Quantum Crystallographic Perspective. *Acta Crystallogr., Sect. B: Struct. Sci. Cryst. Eng. Mater.* **2021**, *77* (4), 478–487. https://doi.org/10.1107/s2052520621005928.

(67) Stash, A. I.; Terekhova, E. O.; Ivanov, S. A.; Tsirelson, V. G. X-Ray Diffraction Study of the Atomic Interactions, Anharmonic Displacements and Inner-Crystal Field in Orthorhombic KNbO 3. *Acta Crystallogr., Sect. B: Struct. Sci. Cryst. Eng. Mater.* **2021**, *77* (5), 728–739. https://doi.org/10.1107/S2052520621006892.

(68) Koritsánszky, T.; Flaig, R.; Zobel, D.; Krane, H. G.; Morgenroth, W.; Luger, P. Accurate Experimental Electronic Properties of DL-Proline Monohydrate Obtained within 1 Day. *Science* **1998**, *279* (5349), 356–358. https://doi.org/10.1126/science.279.5349.356.

(69) Muzet, N.; Guillot, B.; Jelsch, C.; Howard, E.; Lecomte, C. Electrostatic Complementarity in an Aldose Reductase Complex from Ultra-High-Resolution Crystallography and First-Principles Calculations. *Proc. Natl. Acad. Sci.* **2003**, *100* (15), 8742–8747. https://doi.org/10.1073/pnas.1432955100.

(70) Yearley, E. J.; Zhurova, E. A.; Zhurov, V. V.; Pinkerton, A. A. Binding of Genistein to the

Estrogen Receptor Based on an Experimental Electron Density Study. *J. Am. Chem. Soc.* **2007**, *129* (48), 15013–15021. https://doi.org/10.1021/ja075211j.

(71) Flierler, U.; Leusser, D.; Ott, H.; Kehr, G.; Erker, G.; Grimme, S.; Stalke, D. Catalytic Abilities of [(C 6 F 5) 2 BR] (R=NC 4 H 4 and NC 4 H 8) Deduced from Experimental and Theoretical Charge-Density Investigations. *Chem. Eur. J.* **2009**, *15* (18), 4595–4601. https://doi.org/10.1002/chem.200802344.

(72) Liebschner, D.; Elias, M.; Moniot, S.; Fournier, B.; Scott, K.; Jelsch, C.; Guillot, B.; Lecomte, C.; Chabrière, E. Elucidation of the Phosphate Binding Mode of DING Proteins Revealed by Subangstrom X-Ray Crystallography. *J. Am. Chem. Soc.* **2009**, *131* (22), 7879–7886. https://doi.org/10.1021/ja901900y.

(73) Zhurova, E. A.; Zhurov, V. V.; Chopra, D.; Stash, A. I.; Pinkerton, A. A. 17α-Estradiol·1/2 H2O: Super-Structural Ordering, Electronic Properties, Chemical Bonding, and Biological Activity in Comparison with Other Estrogens. *J. Am. Chem. Soc.* **2009**, *131* (47), 17260–17269. https://doi.org/10.1021/ja906057z.

(74) Liu, S.; Rong, C.; Lu, T. Electronic Forces as Descriptors of Nucleophilic and Electrophilic Regioselectivity and Stereoselectivity. *Phys. Chem. Chem. Phys.* **2017**, *19* (2), 1496–1503. https://doi.org/10.1039/C6CP06376D.

(75) Shi, M. W.; Thomas, S. P.; Hathwar, V. R.; Edwards, A. J.; Piltz, R. O.; Jayatilaka, D.; Koutsantonis, G. A.; Overgaard, J.; Nishibori, E.; Iversen, B. B.; Spackman, M. A. Measurement of Electric Fields Experienced by Urea Guest Molecules in the 18-Crown-6/Urea (1:5) Host–Guest Complex: An Experimental Reference Point for Electric-Field-

Assisted Catalysis. *J. Am. Chem. Soc.* **2019**, *141* (9), 3965–3976. https://doi.org/10.1021/jacs.8b12927.

(76) Vuković, V.; Piteša, T.; Jelsch, C.; Wenger, E.; Molčanov, K. An Unusual Intermolecular Interaction between a Lone Pair and an Electron-Rich π-Electron System of a Quinoid Dianion. *Cryst. Growth Des.* **2021**, *21* (10), 5651–5658. https://doi.org/10.1021/acs.cgd.1c00492.

(77) Kohout, M.; Savin, A.; Preuss, H. Contribution to the Electron Distribution Analysis. I. Shell Structure of Atoms. *J. Chem. Phys.* **1991**, *95* (3), 1928–1942. https://doi.org/10.1063/1.460989.

(78) Kohout, M. Occupation Numbers for Atomic Shells in Direct Space Bounded by the Maxima of the One-Electron Potential. *Int. J. Quantum Chem.* **2001**, *83* (6), 324–331. https://doi.org/10.1002/qua.1071.

(79) Shteingolts, S. A.; Fayzullin, R. R. X-Ray Charge Density Study of the Drug Methimazole with Z′ = 2: Differences in the Electronic Structure of the Thiourea Core Due to Crystal Packing Effects. *Cryst. Growth Des.* **2020**, *20* (3), 2074–2090. https://doi.org/10.1021/acs.cgd.9b01715.

(80) Martin, A.; Pinkerton, A. A. Charge Density Studies Using CCD Detectors: Oxalic Acid at 100 K Revisited. *Acta Crystallogr., Sect. B: Struct. Sci.* **1998**, *54* (4), 471–477. https://doi.org/10.1107/S0108768197014596.

(81) Tsirelson, V.; Stash, A.; Kohout, M.; Rosner, H.; Mori, H.; Sato, S.; Lee, S.; Yamamoto, A.; Tajima, S.; Grin, Y. Features of the Electron Density in Magnesium Diboride:

Reconstruction from X-Ray Diffraction Data and Comparison with TB-LMTO and FPLO Calculations. *Acta Crystallogr. Sect. B Struct. Sci.* **2003**, *59* (5), 575–583. https://doi.org/10.1107/S0108768103012072.

(82) Bader, R. F. W.; Essén, H. The Characterization of Atomic Interactions. *J. Chem. Phys.* **1984**, *80* (5), 1943–1960. https://doi.org/10.1063/1.446956.

(83) Espinosa, E.; Alkorta, I.; Elguero, J.; Molins, E. From Weak to Strong Interactions: A Comprehensive Analysis of the Topological and Energetic Properties of the Electron Density Distribution Involving X-H···F-Y Systems. *J. Chem. Phys.* **2002**, *117* (12), 5529–5542. https://doi.org/10.1063/1.1501133.

(84) Bartashevich, E.; Tsirelson, V. A Comparative View on the Potential Acting on an Electron in a Molecule and the Electrostatic Potential through the Typical Halogen Bonds. *J. Comput. Chem.* **2018**, *39* (10), 573–580. https://doi.org/10.1002/jcc.25112.

(85) Levina, E. O.; Khrenova, M. G.; Tsirelson, V. G. The Explicit Role of Electron Exchange in the Hydrogen Bonded Molecular Complexes. *J. Comput. Chem.* **2021**, *42* (12), 870–882. https://doi.org/10.1002/jcc.26507.

(86) Stash, A. I.; Tsirelson, V. G. Developing WinXPRO: A Software for Determination of the Multipole-Model-Based Properties of Crystals. *J. Appl. Crystallogr.* **2014**, *47* (6), 2086–2089. https://doi.org/10.1107/S1600576714021566.

(87) Kamiński, R.; Domagała, S.; Jarzembska, K. N.; Hoser, A. A.; Sanjuan-Szklarz, W. F.; Gutmann, M. J.; Makal, A.; Malińska, M.; Bąk, J. M.; Woźniak, K. Statistical Analysis of Multipole-Model-Derived Structural Parameters and Charge-Density Properties from High-

Resolution X-Ray Diffraction Experiments. *Acta Crystallogr., Sect. A: Found. Adv.* **2014**, *70* (1), 72–91. https://doi.org/10.1107/S2053273313028313.

(88) Volkov, A.; Abramov, Y.; Coppens, P.; Gatti, C. On the Origin of Topological Differences between Experimental and Theoretical Crystal Charge Densities. *Acta Crystallogr., Sect. A: Found. Crystallogr.* **2000**, *56* (4), 332–339. https://doi.org/10.1107/S0108767300003202.

(89) Scherer, W.; Eickerling, G.; Shorokhov, D.; Gullo, E.; McGrady, G. S.; Sirsch, P. Valence Shell Charge Concentrations and the Dewar–Chatt–Duncanson Bonding Model. *New J. Chem.* **2006**, *30* (3), 309–312. https://doi.org/10.1039/b515171f.

(90) Reisinger, A.; Trapp, N.; Krossing, I.; Altmannshofer, S.; Herz, V.; Presnitz, M.; Scherer, W. Homoleptic Silver(I) Acetylene Complexes. *Angew. Chem. Int. Ed.* **2007**, *46* (43), 8295–8298. https://doi.org/10.1002/anie.200702688.

(91) Hebben, N.; Himmel, H.-J.; Eickerling, G.; Herrmann, C.; Reiher, M.; Herz, V.; Presnitz, M.; Scherer, W. The Electronic Structure of the Tris(Ethylene) Complexes [M(C2H4)3] (M=Ni, Pd, and Pt): A Combined Experimental and Theoretical Study. *Chem. Eur. J.* **2007**, *13* (36), 10078–10087. https://doi.org/10.1002/chem.200700885.

(92) Himmel, D.; Trapp, N.; Krossing, I.; Altmannshofer, S.; Herz, V.; Eickerling, G.; Scherer, W. Reply. *Angew. Chem. Int. Ed.* **2008**, *47* (41), 7798–7801. https://doi.org/10.1002/anie.200802616.

(93) Zhao, D.; Yang, Z. Theory on the Molecular Characteristic Contour (I). *Sci. China Ser. B Chem.* **1999**, *42* (4), 391–399. https://doi.org/10.1007/BF02873968.

(94) Zhao, D.; Yan, C.; Zhu, Z.-W.; Zhang, L.; Jiang, Y.-M.; Gong, R.; Yang, Z.-Z. An Intrinsic Criterion of Defining Ionic or Covalent Character of AB-Type Crystals Based on the Turning Boundary Radii Calculated by an Ab Initio Method. *Mol. Phys.* **2018**, *116* (7–8), 969–977. https://doi.org/10.1080/00268976.2017.1418030.

(95) Ospadov, E.; Tao, J.; Staroverov, V. N.; Perdew, J. P. Visualizing Atomic Sizes and Molecular Shapes with the Classical Turning Surface of the Kohn–Sham Potential. *Proc. Natl. Acad. Sci.* **2018**, *115* (50), E11578–E11585. https://doi.org/10.1073/pnas.1814300115.

(96) Wagner, F. R.; Baranov, A. I.; Grin, Y.; Kohout, M. A Position-Space View on Chemical Bonding in Metal Diborides with AlB 2 Type of Crystal Structure. *Z. Anorg. Allg. Chem.* **2013**, *639* (11), 2025–2035. https://doi.org/10.1002/zaac.201200523.

(97) Bartashevich, E. V.; Matveychuk, Y. V.; Mukhitdinova, S. E.; Sobalev, S. A.; Khrenova, M. G.; Tsirelson, V. G. The Common Trends for the Halogen, Chalcogen, and Pnictogen Bonds via Sorting Principles and Local Bonding Properties. *Theor. Chem. Accounts* **2020**, *139* (2), 26. https://doi.org/10.1007/s00214-019-2534-y.

(98) Stash, A.; Tsirelson, V. WinXPRO: A Program for Calculating Crystal and Molecular Properties Using Multipole Parameters of the Electron Density. *J. Appl. Crystallogr.* **2002**, *35* (3), 371–373. https://doi.org/10.1107/S0021889802003230.

(99) Stash, A. I.; Tsirelson, V. G. Modern Possibilities for Calculating Some Properties of Molecules and Crystals from the Experimental Electron Density. *Crystallogr. Reports* **2005**, *50* (2), 177–184. https://doi.org/10.1134/1.1887890.

(100) Mata, I.; Alkorta, I.; Espinosa, E.; Molins, E. Relationships between Interaction Energy, Intermolecular Distance and Electron Density Properties in Hydrogen Bonded Complexes under External Electric Fields. *Chem. Phys. Lett.* **2011**, *507* (1–3), 185–189. https://doi.org/10.1016/j.cplett.2011.03.055.

(101) Kirzhnits, D. Quantum Corrections To the Thomas-Fermi Equation. *Sov. Phys. JETP* **1957**, *Vol: 5*, 64–72.

(102) Becker, P.; Coppens, P. About the Coulomb Potential in Crystals. *Acta Crystallogr., Sect. A* **1990**, *46* (4), 254–258. https://doi.org/10.1107/S0108767389012055.

(103) Su, Z.; Coppens, P. On the Mapping of Electrostatic Properties from the Multipole Description of the Charge Density. *Acta Crystallogr., Sect. A* **1992**, *48* (2), 188–197. https://doi.org/10.1107/S0108767391009820.

(104) Levy, M.; Perdew, J. P.; Sahni, V. Exact Differential Equation for the Density and Ionization Energy of a Many-Particle System. *Phys. Rev. A* **1984**, *30* (5), 2745–2748. https://doi.org/10.1103/PhysRevA.30.2745.

(105) Von Barth, U.; Hedin, L. A Local Exchange-Correlation Potential for the Spin Polarized Case. I. *J. Phys. C Solid State Phys.* **1972**, *5* (13), 1629–1642. https://doi.org/10.1088/0022-3719/5/13/012.

(106) Van Leeuwen, R.; Baerends, E. J. Exchange-Correlation Potential with Correct Asymptotic Behavior. *Phys. Rev. A* **1994**, *49* (4), 2421–2431. https://doi.org/10.1103/PhysRevA.49.2421.

(107) Becke, A. D. Density-Functional Exchange-Energy Approximation with Correct Asymptotic Behavior. *Phys. Rev. A* **1988**, *38* (6), 3098–3100. https://doi.org/10.1103/PhysRevA.38.3098.

(108) Gatti, C.; Saunders, V. R.; Roetti, C. Crystal Field Effects on the Topological Properties of the Electron Density in Molecular Crystals: The Case of Urea. *J. Chem. Phys.* **1994**, *101* (12), 10686–10696. https://doi.org/10.1063/1.467882.

(109) Lu, T.; Chen, F. Multiwfn: A Multifunctional Wavefunction Analyzer. *J. Comput. Chem.* **2012**, *33* (5), 580–592. https://doi.org/10.1002/jcc.22885.

For Table of Contents Use Only

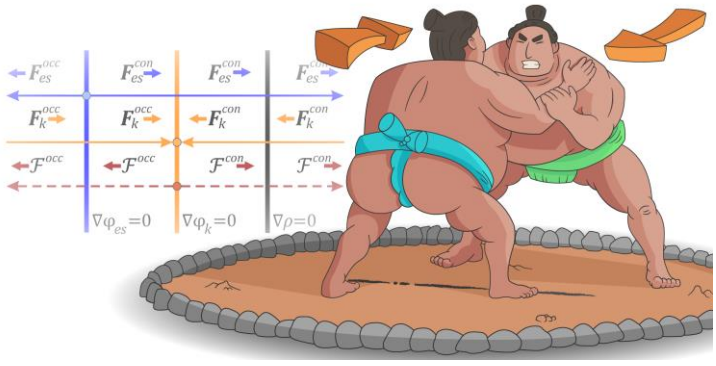

Behavior of one-electron potentials included in the Euler equation for electron density and corresponding gradient force fields in crystals was studied. Phenomena of interatomic charge transfer and consequent electron exchange were explained in terms of space gaps between the zero-flux surfaces of atomic and electrostatic and kinetic potential-based basins.